Measurement of the $t\bar{t}\gamma\gamma$ production cross-section in pp collisions at a center-of-mass-energy of $\sqrt{s} = 13$ TeV with the ATLAS detector at the LHC

MASTERARBEIT

zur Erlangung des akademishen Grades

Master of Science

(M.Sc)

der Universität Siegen

Naturwissenschaftlich Technische Fakultät

Department Physik

vorgelegt von

Nomin-Erdene Erdenebat

im Juni 2018

Contents

Chapter 1

Introduction

Measurements of the top-quark properties play an important role in testing the Standard Model (SM) due to its heavy mass close to the electroweak breaking scale and short life time. It also has an important role in the study of the background processes (e.g. Higgs Boson Physics) at the Large Hadron Collider (LHC). In many scenarios beyond the SM heavier particles decay into the top quarks. Studying detailed properties of the top quarks can give handles on new physics. Since there are the large number of $t\bar{t}$ pairs produced during the LHC Run 2, this high statistics will allow to measure the properties of the top quark precisely. In particular, the production of a top-quark pair in association with two photons ($t\bar{t}\gamma\gamma$) can probe the electroweak coupling between the top quark and photons.

In this thesis a measurement of the $t\bar{t}\gamma\gamma$ production cross-section is performed with data collected by the ATLAS detector during 2015 and 2016 corresponding to an integrated luminosity of 36.1 fb^{-1} at a center-of-mass-energy of $\sqrt{s} = 13$ TeV, in the single lepton channels. The final state of the $t\bar{t}\gamma\gamma$ process is similar to the $t\bar{t}\gamma$ process, but it contains two prompt photons. So, this analysis is built on the single-lepton $t\bar{t}\gamma$ analysis [17] in ATLAS. In the single lepton channels, one lepton and at least four jets are requested, with at least one jet being b-tagged and two isolated photons with $p_T > 20$ GeV and $|\eta| < 2.37$. The event yields and kinematic distributions are compared between data and MC in the signal region.

This thesis is structured as follows: In Chapter 2 an overview of the standard model and the basic concepts of the top-quarks physics are introduced. The Chapter 3

describes the ATLAS experiment at the LHC and its detector components. Then, the measurement of the $t\bar{t}\gamma\gamma$ production cross-section is discussed in Chapter 4. Further, the kinematic distributions, background and systematic uncertainty studies are presented. Finally, the last chapter will summarize the thesis and give an outlook.

Chapter 2

Theoretical Overview

2.1 The Standard Model of Particle Physics

The Standard Model explains how the basic building blocks of matter interact with each other through the four fundamental forces. According to this model, all matter is made out of elementary particles, the building blocks of matter. These particles occur in two basic types called quarks and leptons (spin $\frac{1}{2}$ particles, or fermions). Each group consists of six particles, which are related in pairs, or "generations". In the **Table 2.1** the charge and mass of these quarks and leptons corresponding to the three generations are included. As shown in the **Figure 2.1**, the electron neutrino (ν_e), the electron (e^-), down-quark (d) and the up-quark (u) make up the first generation. So, the lightest and most stable particles make up the first generation, whereas the heavier and less stable particles belong to the second and third generations.

There are also six anti-leptons and anti-quarks, with all the signs reversed. For instance, the positron carries a charge of +1e and an electron -1e, with $e = 1.602176565(35) \times 10^{19}$ C. But quarks and anti-quarks carry non-integer electric charge, being (+2/3 e) or (-1/3 e) and they also come in three colors, so there are 36 of them in all. Totally there are 12 leptons and 36 quarks including the anti-particles.

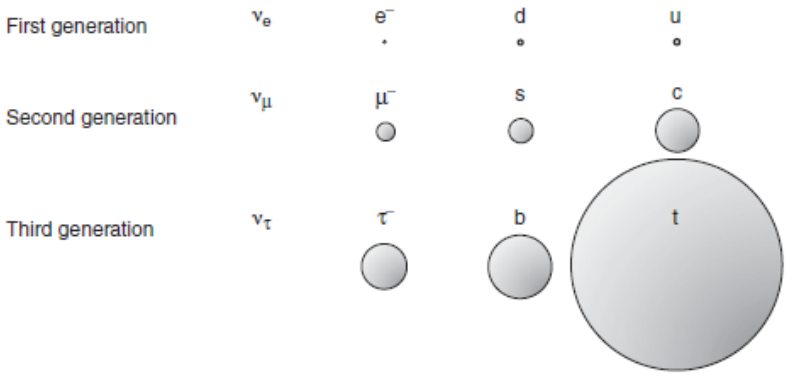

Figure 2.1 The particles in the three generations of fundamental fermions with the masses indicated by imagined spherical volumes of constant density [1].

Table 2.1 The twelve fundamental fermions divided into quarks and leptons.

	Leptons			Quarks		
	Particle	Q	mass/GeV	Particle	Q	mass/GeV
First	electron (e^-)	-1	0.0005	down (d)	-1/3	0.003
generation	neutrino (ν_e)	0	$< 10^{-9}$	up (u)	+2/3	0.005
Second	muon (μ^-)	-1	0.106	strange (s)	-1/3	0.1
generation	neutrino (ν_μ)	0	$< 10^{-9}$	charm (c)	+2/3	1.3
Third	tau (τ^-)	-1	1.78	bottom (b)	-1/3	4.5
generation	neutrino (ν_τ)	0	$< 10^{-9}$	top (t)	+2/3	174

In addition, every interaction has its mediators: the photon for the electromagnetic force, two W's and a Z boson for the weak force, the graviton for gravity and the gluon for the strong force, respectively. In the next Section these four forces and mediators are discussed in detail.

2.2 The Fundamental Forces

Particles interact with each other through the four fundamental forces: strong, weak, electromagnetism and gravity. The gravitational force between two individual particles is extremely small and can be neglected in the discussion of particle interactions. **Table 2.2** shows the strength and mediators corresponding to these forces. They are listed in order of decreasing strength.

Table 2.2 The four known forces of nature.

Force	Strength	Boson	Spin	mass/GeV
Strong	1	Gluon g	1	0
Electromagnetism	10^{-3}	Photon γ	1	0
Weak	10^{-8}	W boson $W^{\pm}$	1	80.4
		Z boson Z	1	91.2
Gravity	10^{-37}	Graviton G	2	0

Each of three forces is described by a Quantum Field Theory (QFT) corresponding to the exchange of a spin-1 force carrying particle, know as a gauge boson. The familiar spin-1 photon is the gauge boson of Quantum Electrodynamics (QED). In the case of the strong interaction, the force-carrying particle is called the gluon which, like the photon, is massless. The weak charged-current interaction, which is responsible for nuclear β-decay and nuclear fusion, is mediated by the charged W^+ and W^- bosons, which are approximately eighty times more massive than the proton. There is also a weak neutral-current interaction, closely related to the charged current, which is mediated by the electrically neutral Z boson. These gauge bosons couple to the spin-half fermions. The coupling of the gauge bosons to the fermions is described by the SM interaction vertices, as shown in the **Figure 2.2**. In each case, the interaction is a three-point vertex of the gauge boson and an incoming and outgoing fermion.

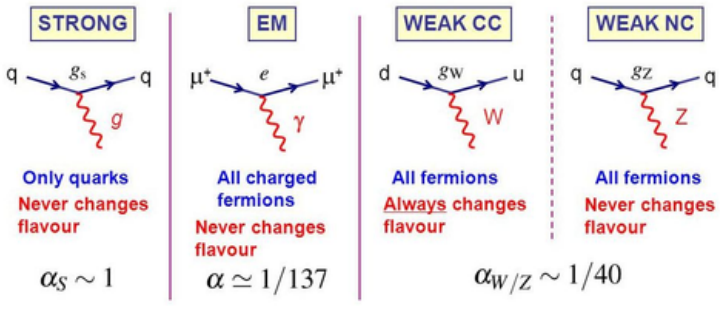

Figure 2.2 The Standard Model interaction vertices [1].

For each type of interaction there is an associated coupling strength g. For example, for QED the coupling strength is simply the electron charge, $g_{QED} = e$. In

Table 2.3 The forces experienced by different particles [1].

					Strong	Electromagnetic	Weak
Quarks	down-type	d	s	b	✓	✓	✓
	up-type	u	c	t			
Leptons	charged	e^-	μ^-	τ^-		✓	✓
	neutrinos	ν_e	ν_μ	ν_τ			✓

the **Table 2.3** the properties of the fundamental fermions are categorized by the types of interaction.

All twelve fundamental particles "feel" the weak force and undergo weak interactions. With the exception of the neutrinos, which are electrically neutral, the other nine particles are electrically charged and participate in the electromagnetic interaction of QED. Only the quarks carry the QCD equivalent of electric charge, called colour charge. Consequently, only the quarks feel the strong force. Because of the nature of the QCD interaction, quarks are never observed as free particles, but are always confined to bound states called hadrons, such as the proton and neutron. Because the quarks feel the strong force, their properties are very different from those of the electron, muon, tau-lepton and the neutrinos, which are collectively referred to as the leptons.

2.2.1 Quantum Electrodynamics (QED)

The QED is the QFT of the electromagnetic interaction, where the interactions between charged particles are mediated by virtual photons. As an example, the following figure shows the diagram in which the electrons exchange a photon.

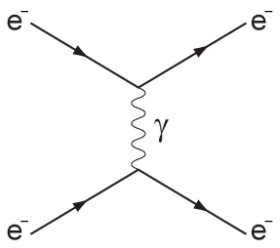

Here, two electrons enter, a photon passes between them (one emits the photon and another one absorbs it) and the two exit. This process is called Moller scattering which is mediated by the exchange of a photon.

As another example, consider the following diagram of the annihilation process:

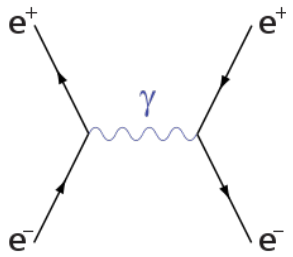

Here, an electron and a positron annihilate to form a photon, which in turn produces a new electron-positron pair. This represents the interaction of two opposite charges. This process is called the Bhabha scattering.

We can also construct the following diagrams by using two vertices:

pair annihilation: $e^- + e^+ \longrightarrow \gamma + \gamma$,
pair production: $\gamma + \gamma \longrightarrow e^- + e^+$,
Compton scattering: $e^- + \gamma \longrightarrow e^- + \gamma$

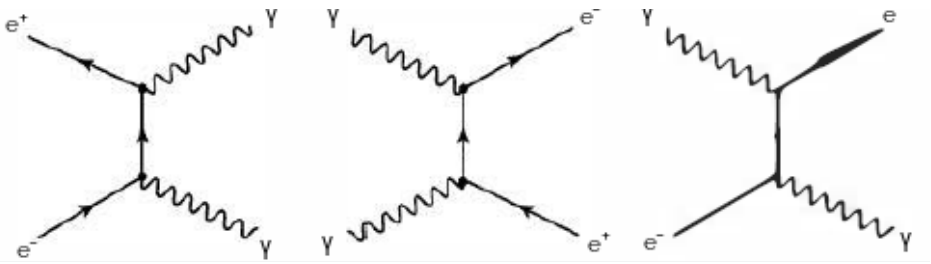

2.2.2 Quantum Chromodynamics (QCD)

The QCD is the QFT of the strong force. It describes the interactions between coloured particles which are mediated by the exchange of gluons. As mentioned in the previous Section, the quarks carrying the colour charge (red r, blue b and green g) exist in three colour state. Similarly, the antiquarks carry the opposite

colour charge to the quarks ($\bar{r}$, $\bar{b}$ and $\bar{g}$). Since leptons do not carry color, they do not participate in the strong interaction. The fundamental process in the QCD is quark→quark plus gluon ($q \longrightarrow q + g$) as shown in the following diagram:

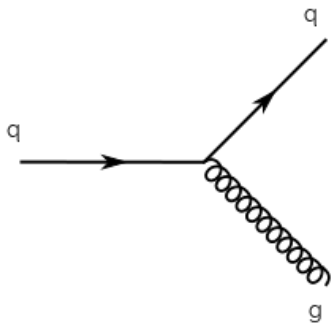

In this process, the colour of the quark(but not its flavor) may change. As another example, consider more complicated process in which the force between two quarks is described in lowest order:

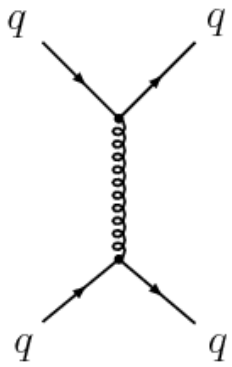

Here, the force between two quarks is mediated by the exchange of gluons. Since color (like charge) is always conserved, this means that the gluon must carry colour. Also there are three-gluon vertices and four-gluon vertices as shown the following diagrams:

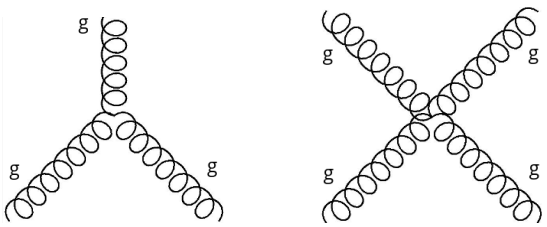

In addition there is difference of the size of the coupling constant between chromodynamics and electrodynamics. Each vertex in the QED introduces $\alpha = 1/137$, and experimentally the corresponding coupling constant for strong force is greater than 1 [2].

2.2.3 Weak Interactions

All leptons and all quarks participate in the weak interactions. There are two kinds of weak interactions: charged (mediated by the W's) and neutral (mediated by the Z).

Leptons:

The fundamental charged vertex looks like as shown in the **Figure 2.3a**. A negative lepton (e^- , μ^- or τ^-) converts into the corresponding neutrino, with emission of a W^- (or absorbtion of a W^+): $l \longrightarrow \nu_l + W^-$. An example in the **Figure 2.3b** shows the $\mu^- + \nu_e \longrightarrow e^- + \nu_\mu$ process which is mediated by the W^- boson:

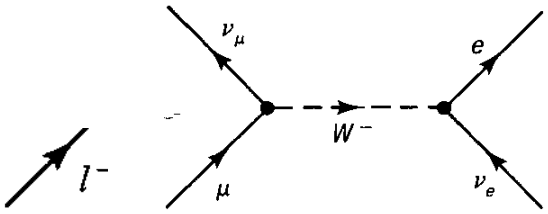

(a) (b)

Figure 2.3 a. The fundamental charged vertex b. $\mu^- + \nu_e \longrightarrow e^- + \nu_\mu$ process

As shown in the **Figure 2.4a**, the fundamental neutral vertex looks like. In this case l can be any lepton (including neutrinos). The Z boson mediates such processes as the $\nu_\mu + e^- \longrightarrow \nu_\mu + e^-$ process in the **Figure 2.4b**:

Quarks:

The fundamental charged vertex is shown in the **Figure 2.5a**. A quark with charge $-\frac{1}{3}$ (d, s, or b) converts into the corresponding quark with charge $+\frac{2}{3}$ (u,

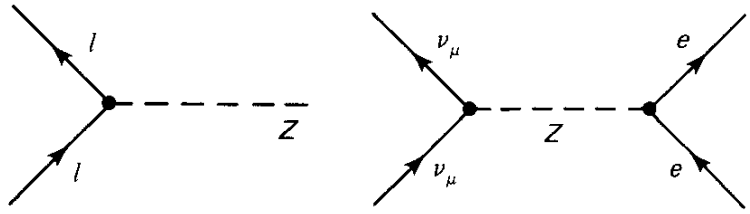

(a) (b)

Figure 2.4 a. The fundamental neutral vertex b. $\nu_\mu + e^- \longrightarrow \nu_\mu + e^-$ process

c, or t, respectively), with the emission of a W^-. The outgoing quark cames the same colour as the ingoing one, but a different flavour. As an example, consider the following semileptonic process in the **Figure 2.5b**:

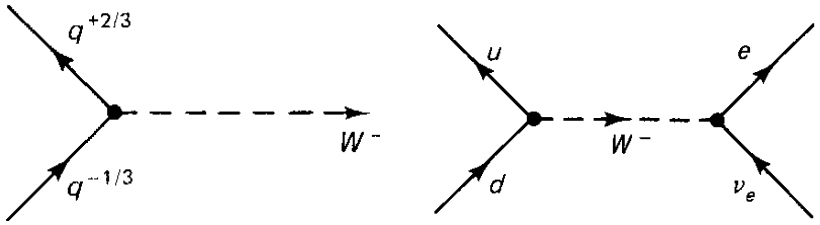

(a) (b)

Figure 2.5 a. The fundamental charged vertex b. the semileptonic process

Because of quark confinement, this process would never occur in nature [2]. The fundamental neutral vertex for quarks is shown in the **Figure 2.6a**. This leads to the $\nu_\mu + p \longrightarrow \nu_\mu + p$ process in the **Figure 2.6b**:

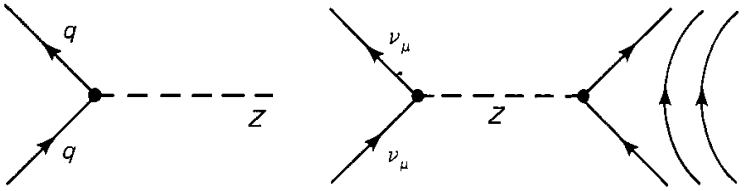

(a) (b)

Figure 2.6 a. The fundamental neutral vertex b. the $\nu_\mu + p \longrightarrow \nu_\mu + p$ process

Also there is a neutrino-electron scattering which is a purely leptonic process where a neutrino scatters off an electron by the exchange of a virtual vector boson.

Finally, the weak interactions of quarks are described in terms of the unitary Cabibbo-Kobayashi-Maskawa (CKM) matrix. The weak eigenstates are related to the mass eigenstates by the following matrix:

$$\begin{pmatrix} d' \\ s' \\ b' \end{pmatrix} = \begin{pmatrix} V_{ud} & V_{us} & V_{ub} \\ V_{cd} & V_{cs} & V_{cb} \\ V_{td} & V_{ts} & V_{tb} \end{pmatrix} \cdot \begin{pmatrix} d \\ s \\ b \end{pmatrix} \tag{2.1}$$

2.3 Top Quark Production

The heaviest known elementary particle, the top quark, was discovered in 1995 by the CDF and D0 collaborations at the Tevatron proton-antiproton collider at Fermilab. In 2010 it was re-discovered at the LHC. With approximately 3.5 times higher center-of-mass energy compared to the Tevatron, cross sections for top-quark production are more than 20 times higher than at the Tevatron [3].

Top quarks are produced mainly in pairs via the strong interactions at the LHC. At parton level two leading order (LO) processes contribute that lead to $t\bar{t}$ final states: gluon-gluon (gg) fusion in the s-, t-, and u-channel and quark-antiquark ($q\bar{q}$) annihilation processes in the **Figure 2.7**. In proton-proton collisions, $q\bar{q}$ annihilation can take place between valence quarks or sea quarks and sea antiquarks.

In the LHC at a center-of-mass energy of $\sqrt{s} = 13$ TeV, $t\bar{t}$ production is dominated by gg fusion (approximately 90%), while only 10% of the $t\bar{t}$ pairs are produced via $q\bar{q}$ annihilation [3]. In addition to the pair production, there is the single top production via the weak interaction. The inclusive cross section is about two to three times smaller than for strong $t\bar{t}$ production.

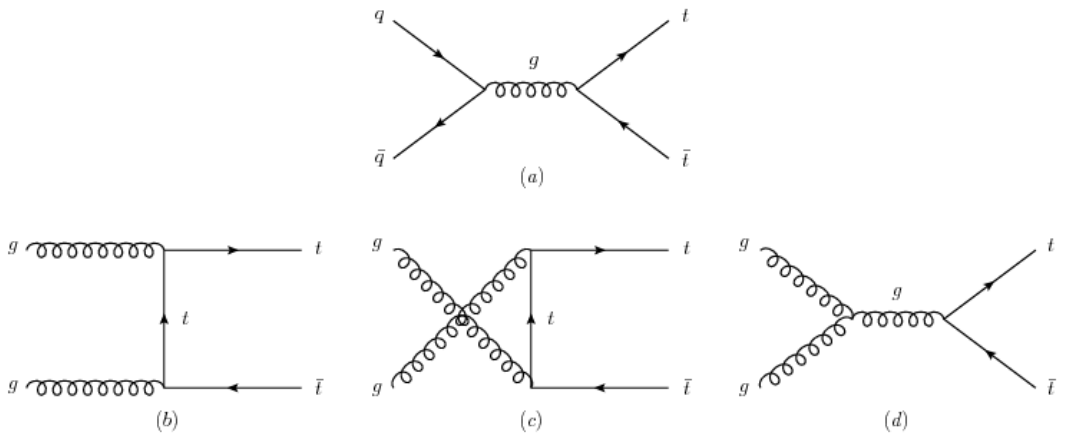

Figure 2.7 Feynman diagrams for $t\bar{t}$ production in the QCD at the LO: $q\bar{q}$ annihilation (top), gg fusion in the t-channel (bottom left), and gg fusion in the u-channel (bottom middle), gg fusion in the s-channel (bottom right).

The production processes are classified by the virtuality of the W boson exchanged in the processes.

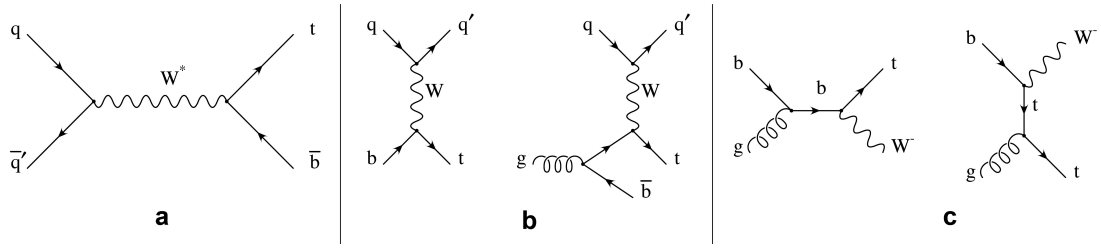

Figure 2.8 Feynman diagrams for electroweak single top-quark production at the LO: a. s-channel production, b. t-channel production in the four-favour scheme and five-favour scheme, and c. associated Wt production.

The most abundant single top-quark production process at the LHC is t-channel production (SM expectation: 70% of the total cross section), followed by the associated production of a top quark and a real W boson (25%), and s-channel production (5%) [3].

2.4 Top Quark Decays

The top quark decays via the electroweak charged-current process $t \to W^+q$, where q is a down-type quark (down, strange, or bottom). The collision events containing $t\bar{t}$ pairs are classified by the decay of the W^+ and the W^- boson from the $t\bar{t}$ decay. The $W^+(W^-)$ bosons decay into hadronic final states $q\bar{q}'$ with a branching fraction of approximately 2/3 and into a charged lepton $l^+(l^-)$ and its corresponding (anti)neutrino $\nu_l(\bar{\nu}_l)$ with a branching fraction of approximately 1/3 or 1/9 per lepton flavour [3]. This results in the following classification scheme for $t\bar{t}$ decay channels:

- Fully hadronic (also: all-hadronic, all-jets) channel:

  $t\bar{t} \to W^+bW^-\bar{b} \to q\bar{q}'bq"q"\bar{b}$,
- Single-lepton (also: lepton+jets, semileptonic) channel:

  $t\bar{t} \to W^+bW^-\bar{b} \to l^+\nu_l bq\bar{q}'\bar{b}$ and $t\bar{t} \to W^+bW^-\bar{b} \to q\bar{q}'\bar{b}l^-\bar{\nu}_l\bar{b}$,
- Dilepton channel:

  $t\bar{t} \to W^+bW^-\bar{b} \to l^+\nu_l bl^{-'}\bar{\nu}_{l'}\bar{b}$,

Also in the **Figure 2.9** all possible final states of the decay of a top-quark pair are shown.

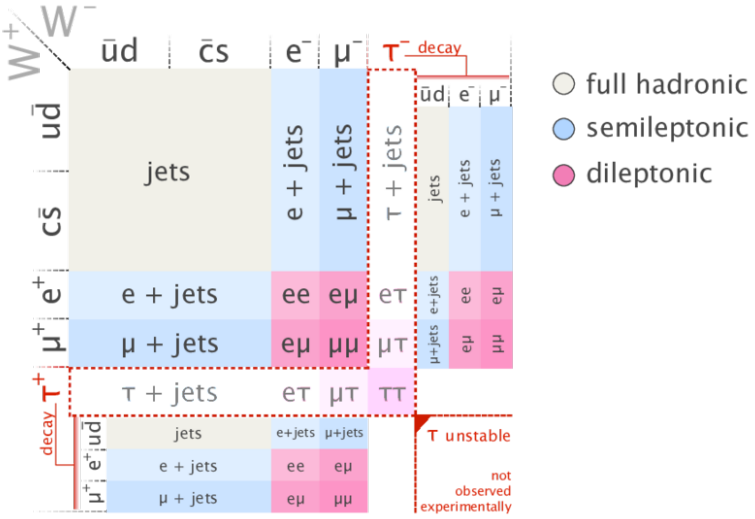

Figure 2.9 All possible final states of the decay of the $t\bar{t}$ [4].

The considered final states are the single lepton channels ($e + jets$ and $\mu + jets$) and dilepton channels (ee, $e\mu$, $\mu\mu$), including electrons and muons from possible leptonic lepton decay. The fully hadronic channel has the largest branching fraction of $(2/3)^2 \simeq 0.45$ but also suffers from the largest background. The single-lepton channel with its moderate branching fraction of $2 \times 2/3 \times (2 \times 1/9) \simeq 0.29$ has moderate backgrounds, while the dilepton channel has the smallest branching fraction of only $(2 \times 1/9)^2 \simeq 0.05$, but only very small backgrounds [3].

2.5 Radiative Top-Quark Processes

Photons can be radiated during the top quark production as well as the decay process. In the radiative top production via gluon fusion, the photon can only be radiated off the off-shell top quarks. In the radiative top production via quark anti-quark annihilation, the photon can also be radiated off one of the incoming quarks [5]. In the figure 2.10a, some Feynman diagrams for the radiative top production processes are shown.

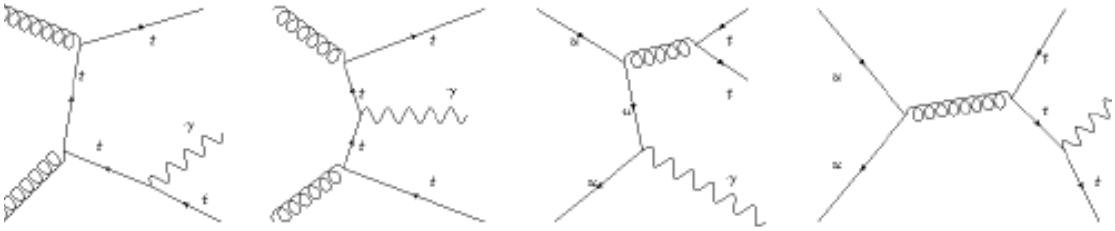

Figure 2.10a : The left two diagrams corresponds to the radiative top quark production processes via gluon fusion and the rest diagrams to the radiative top quark production via quark anti-quark annihilation. Via gluon processes the photon is radiated off the off-shell top quark. In the radiative top production via quark anti-quark annihilation, the photon is emitted by the incoming quarks or by the top quark.

In the radiative top quark decay, the photon can be emitted by the bottom quark or W boson from the top quark decay, or the lepton decayed from the W boson, or

the on-shell top quark. In the figure 2.10b, some Feynman diagrams for radiative top quark decay processes are shown.

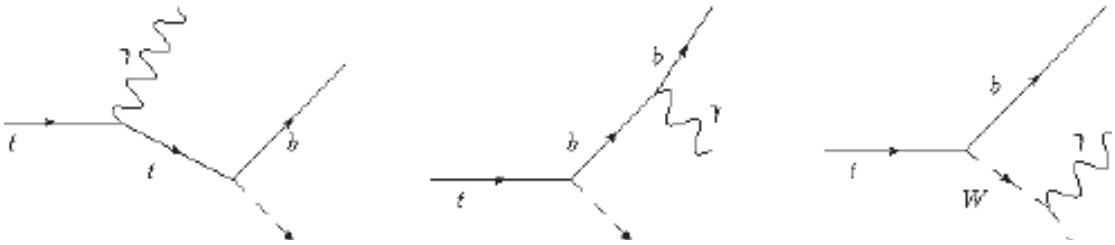

Figure 2.10b The radiative top quark decay processes. The photon can be radiated off the top quark or one of its decay products.

The final state of the $t\bar{t}\gamma\gamma$ process is similar to the final state of the usual top quark pair production, but it contains additional two prompt photons. In this final state, two photons can also be radiated from the top production and the decay process as shown the following diagrams:

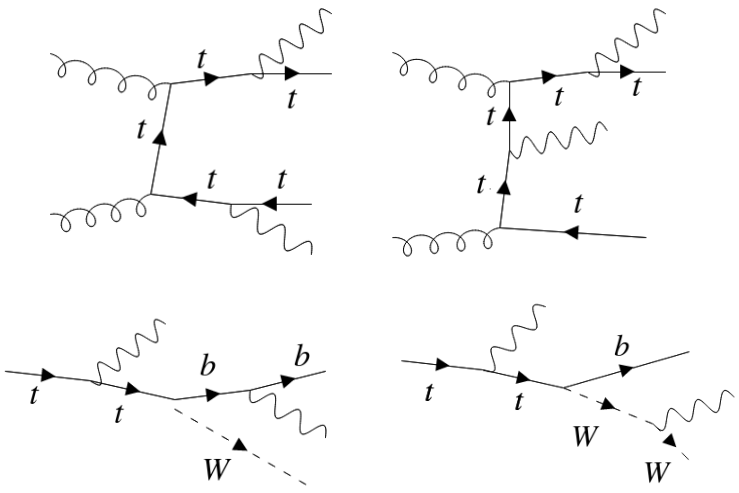

Figure 2.10c In the upper two diagrams two photons are radiated from the top production. In the bottom two diagrams two photons are radiated from the decay process.

Chapter 3

Experimental Setup

This chapter introduces the ATLAS experiment at the LHC and its detector components. The ATLAS experiment investigates a wide range of physics, from the search for the Higgs boson to extra dimensions and particles that could make up dark matter. It is one of two general-purpose detectors at the LHC. Although it has the same scientific goals as the CMS experiment, it uses different technical solutions and a different magnet-system design. Its detailed explanations are given in the Sections 3.2.

In early 2015 the LHC was restarted as Run 2. The center-of-mass energy was increased to 13 TeV, which boosted typical top-quark cross sections by a factor of about three compared to Run 1 [3]. The ATLAS and CMS has recorded the proton-proton collision data equivalent to a luminosity of about 3.21 fb^{-1} in 2015 and 32.88 fb^{-1} in 2016, respectively. At this integrated luminosity, the Run 2 top-quark datasets are already about five times as large as the Run 1 datasets [3]. In this analysis the datasets collected by the ATLAS detector during the 2015 and 2016 are used. In the next Chapter the samples and analysis steps are discussed in detail.

3.1 The Large Hadron Collider

The Large Hadron Collider is the world's biggest and most powerful particle accelerator. It was installed into the existing Large Electron Positron (LEP) tunnel

at the CERN laboratory across the Franco-Swiss border west of Geneva. It first started up on 10 September 2008. The LHC consists of a 27-kilometer ring of superconducting magnets with a number of accelerating structures to boost the energy of the particles along the way. Inside the accelerator, two high-energy proton beams travel at close to the speed of light before they are made to collide. The beams travel in opposite directions in separate beam pipes. As shown **Figure 2.11**, Linac 2, the first accelerator in the chain, accelerates the protons to the energy of 50 MeV. The beam is then injected into the Proton Synchrotron Booster (PSB), which accelerates the protons to 1.4 GeV, followed by the Proton Synchrotron (PS), which pushes the beam to 25 GeV. Protons are then sent to the Super Proton Synchrotron (SPS) where they are accelerated to 450 GeV [6].

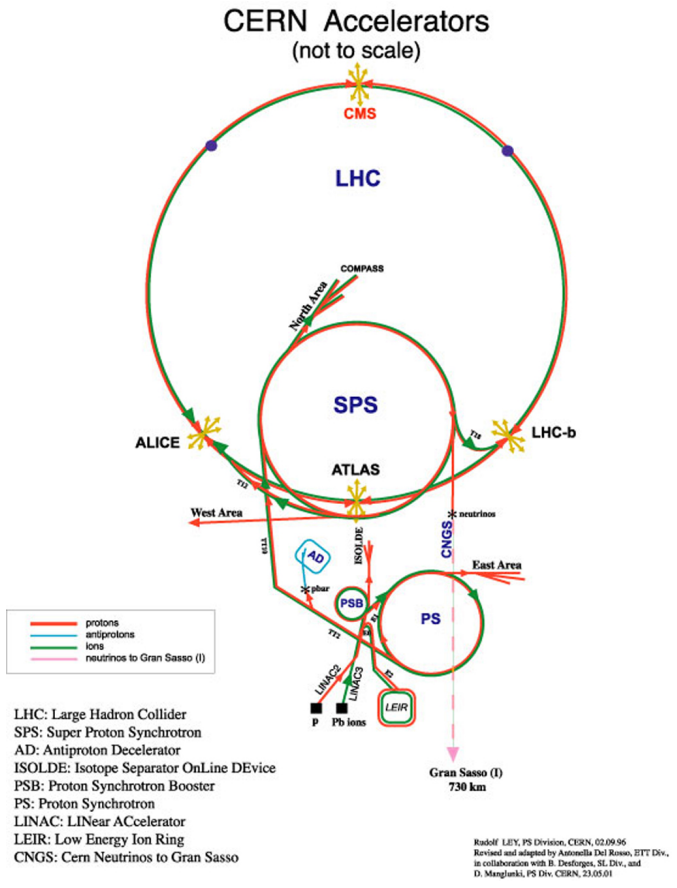

Figure 2.11 The accelerator complex at CERN [7].

The protons are finally transferred to the two beam pipes of the LHC. The beam in one pipe circulates clockwise while the beam in the other pipe circulates anti-

clockwise. Each proton beams are accelerated up to the record energy of 6.5 TeV per beam. Then, two beams are brought into collision inside four detectors - ALICE, ATLAS, CMS and LHCb - where the center-of-mass energy at the collision point is equal to 13 TeV.

The ATLAS and CMS detectors, are large general-purpose particle detectors that study the Higgs boson and looks for signs of new physics, including the origins of mass and extra dimensions. The ALICE detector is an experiment mainly devoted to the quark-gluon plasma study by heavy-ion (Pb) collisions. The LHCb is a specialized b-physics experiment, that is measuring the parameters of CP violation in the interactions of b-hadrons (heavy particles containing a bottom quark).

The luminosity of a collider is expressed as [8]:

$$L = \frac{N^2 k_b f}{4\pi\sigma *_x \sigma *_y} F \tag{3.1}$$

Assuming round beams and equal values of the beta function for both beams in both planes, this may be expressed as:

$$L = \frac{N^2 k_b f \gamma}{4\pi\epsilon_n \beta *} F \tag{3.2}$$

Here:

- N is the number of particles per bunch
- k_b is the number of bunches
- f is the revolution frequency
- γ is the usual relativistic factor
- $\sigma *_x$ and $\sigma *_y$ are the horizontal and vertical beam sizes at the interaction point
- ϵ_n is the normalized emittance
- $\beta *$ is the value of the beta function at the interaction point
- F is the geometrical reduction factor arising from the crossing angle

The corresponding values for these parameters at the peak performance of the LHC are shown in the **Table 3.1**. The design report values are shown for comparison [9].

Table 3.1 Comparison between the main LHC and beam parameters.

Parameter	Design Value	Value in 2015
Beam energy [TeV]	7	6.5
Bunch spacing [ns]	25	25
Number of bunches	2808	2244
Average bunch intensity	1.15×10^{11}	1.15×10^{11}
Transv. emittance [μm]	3.75	3.5
Peak luminosity [$cm^{-2}s^{-1}$]	1×10^{34}	5.0×10^{34}

In 2016, the integrated luminosity delivered by the LHC reached the 2016 target value of $25fb^{-1}$ in both the ATLAS and CMS experiments. The LHC energy for the single beam is currently 6.5TeV instead of the nominal 7TeV.

3.2 The ATLAS Detector

The ATLAS detector has the dimensions of a cylinder, 46m long, 25m in diameter, and sits in a cavern 100m below ground and it weighs 7,000 tonnes. It consists of the four major components: Inner Detector, Calorimeter, Muon Spectrometer and Magnet System as shown in the **Figure 2.12**.

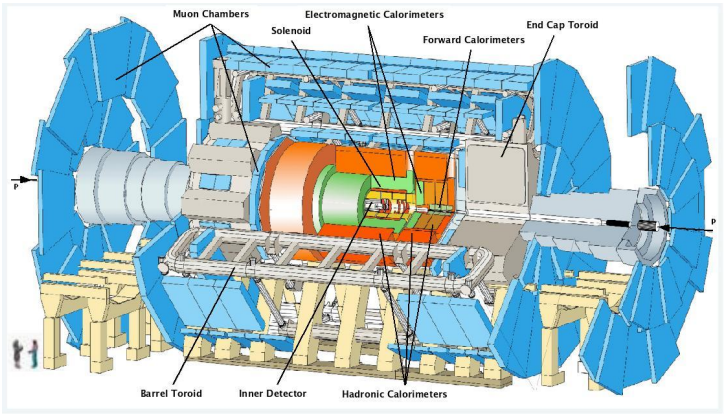

Figure 2.12 A schematic of the ATLAS detector at the LHC.

In the innermost layer, the first tracking detector (the Inner detector), which

measures the position of a crossing charged particle with minimal disturbance, are placed. Then the Calorimeters which measure the energy of a particle by total absorption, divided into the Electromagnetic and Hadronic calorimeters. In the outermost layer the Muon Spectrometer is placed. The Solenoids and Toroids are magnets to bend the charged particles and measure their momentum.

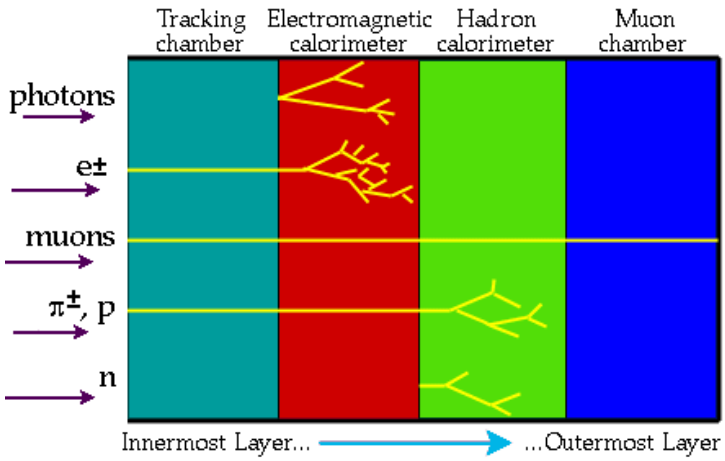

Figure 2.13 Tracks of the charged particles in the Inner silicon tracking chambers [10].

The **Figure 2.13** shows the charged particles of electrons, muons, protons, and pions leaving tracks in the Inner silicon tracking chambers. Then, light electrons and photons make showers leading to their total energy measurement in the Electromagnetic Calorimeter. In the Hadronic Calorimeter, the strongly interacting protons, neutrons, and pions are stopped and their energy measured by their particle showers. Finally, the muon tracks in the Muon chamber with a magnetic field that bends their paths to measure their momentum and energy.

3.2.1 The Coordinate System of ATLAS

The coordinate system in the ATLAS detector is a right-handed coordinate system with the x-axis pointing towards the centre of the LEP/LHC tunnel, and the z-axis along the tunnel. The y-axis is slightly tilted with respect to vertical from the general tilt of the tunnel [11]. The interaction point is defined as the origin of the system.

The coordinate system of ATLAS is shown in **Figure 2.14**. The pseudorapidity of particles from the primary vertex is defined as:

$$\eta = -log(tan\frac{\theta}{2}) \tag{3.3}$$

where θ is the polar angle of the particle direction measured from the positive z-axis. Transverse momentum is defined as the momentum perpendicular to the LHC beam axis.

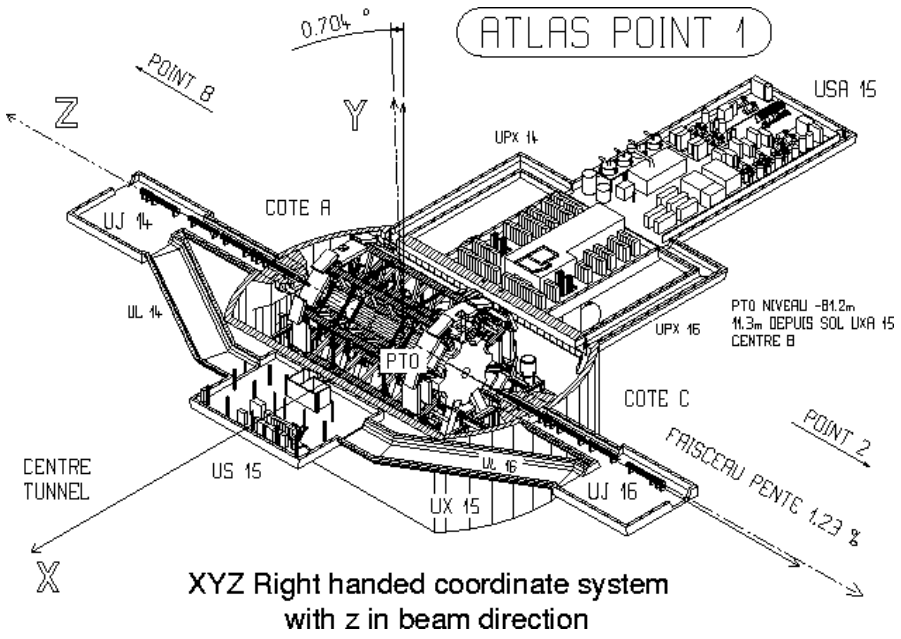

Figure 2.14 The coordinate system in the ATLAS detector. The general tilt of the LEP/LHC tunnel causes the y-axis to be slightly different from vertical [11].

3.2.2 The Inner Detector

The inner detector is the first part of the ATLAS detector to see the decay products of the collisions, so it is very compact and highly sensitive. It consists of three different systems of sensors all immersed in a magnetic field parallel to the beam axis. The Inner Detector measures the direction, momentum, and charge of electrically-charged particles produced in each proton-proton collision.

The main components of the Inner Detector are: Pixel Detector, Semiconductor Tracker (SCT), and Transition Radiation Tracker (TRT).

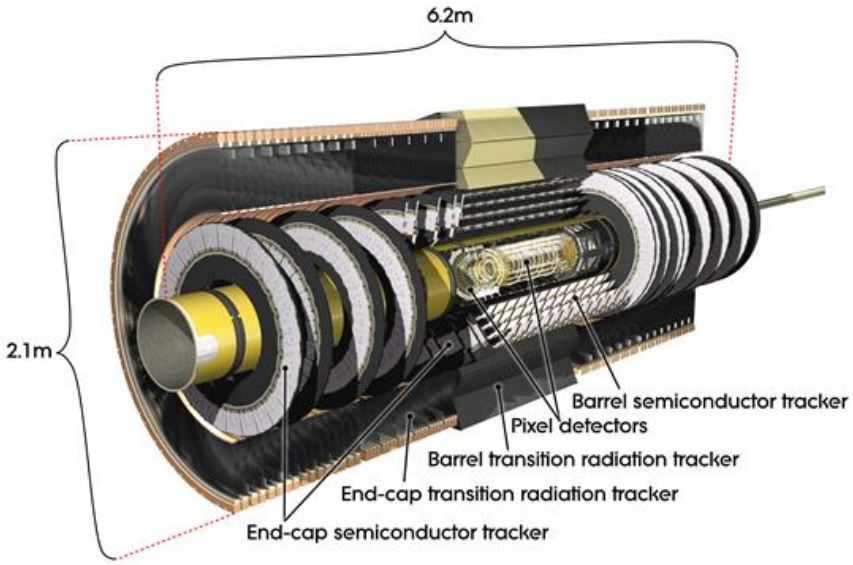

Figure 2.15 The ATLAS Inner Detector.

The Pixel Detector:

The pixel detector is the innermost element of the Inner Detector as shown in **Figure 2.15**. The pixel tracker is designed to provide at least three points on a charged track emanating from the collision region in ATLAS. The pixel detector and the other elements of the Inner Detector span a pseudorapidity range $|\eta| < 2.5$. The principal components of the pixel tracking system are the following components:

• The active region of the pixel detector, which is composed of three barrel layers and a total of six disk layers, three at each end of the barrel region. In addition to the existing three layer, there is a fourth layer of the pixel detector which is called the insertable B-layer (IBL).

• The internal services (power, monitoring, optical input/output and cooling) and their associated mechanical support structures (also supporting the interaction region beam pipe) on both ends of the active detector region,

• The Pixel Support Tube into which the active part of the pixel detector and the services and related support structures are inserted and located,

• The external services that are connected to the internal services at the end of the Pixel Support Tube.

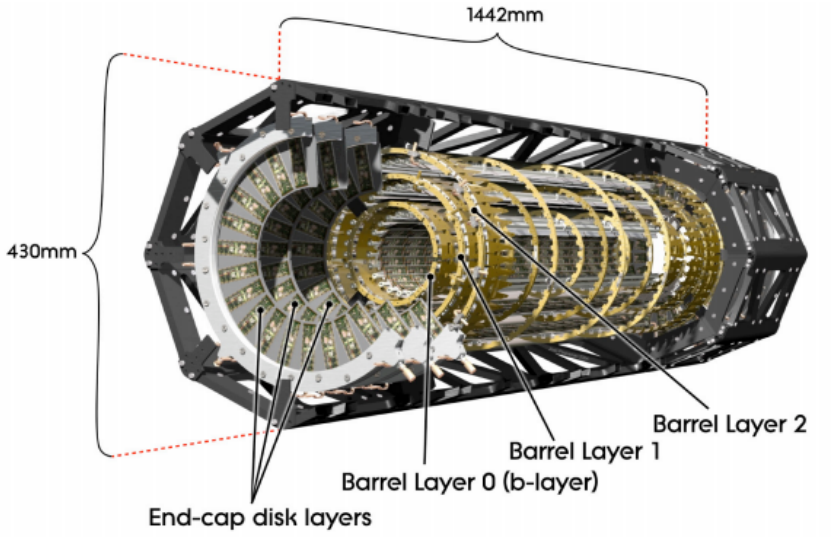

Figure 2.16 A schematic view of the active region of the pixel detector consisting of barrel and endcap layers.

The active region of the pixel detector is shown in the **Figure 2.16**. The active part of the pixel system consists of three barrel layers-Layer 0 (so-called b-layer), Layer 1 and Layer 2-and two identical endcap regions, each with three disk layers.

The two endcap regions are identical. Each is composed of three disk layers, and each disk layer is identical. The total number of pixels in the system is approximately 67 million in the barrel and 13 million in the endcaps, covering a total active area of about 1.7 m^2 [12].

Semiconductor Tracker (SCT)

The SCT detectors use semiconductor technology to provide precision space-point coordinates. It contains 61 m^2 of silicon detectors, with 6.2×10^6 readout channels. In the barrel there are four cylinderical layers of modules, placed at radii of 300, 373, 447, and 520 mm [13]. Each module consists of four detectors. Each silicon

detector is 6.36 cm × 6.40 cm with 768 readout strips of 80 μm pitch. On each side of a module, two detectors are bound together to form 12.8 cm long strips, with a 2 mm dead area in the middle. Two such detector planes are glued together at a 40 mrad angle [13]. This small stereo angle is used to obtain the z-measurement of the (ϕ , r, z) precision points. In the following figure shows the SCT barrel and endcaps with a quadrant view of the Inner detector.

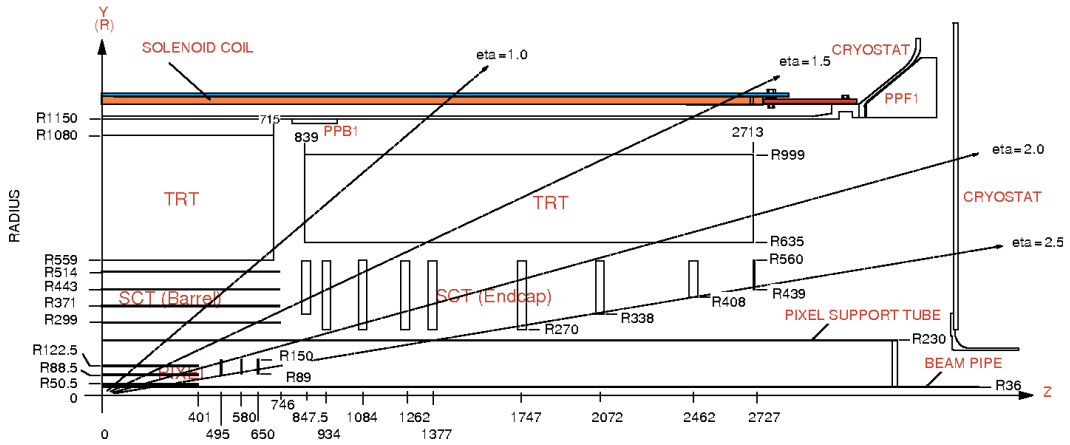

Figure 2.17 A quadrant view of the Inner Detector [14].

In each of the two endcaps there are nine disks, with every layer able to read out a position in two dimensions. End-cap modules are made in two versions with lengths of about 12 and 7 cm. The 12 cm strips consist of two parts, with a 2 mm dead area in the middle [13]. The end-cap modules are mounted in up to three rings onto nine wheels, which are interconnected by a space frame.

Transition Radiation Tracker (TRT):

The Transition Radiation Tracker contributes to the transverse momentum measurement. The TRT is based on the use of straw detectors, which can operate at the required very high rates by virtue of their small diameter and the isolation of the sense wires within individual gas envelopes. A straw tube is a thin cylindrical tube with a conducting inner surface at negative potential.

The barrel section is built of individual modules with between 329 and 793 axial straws each (parallel to the beam direction), covering the radial range from 56 to

107 cm. The total number of straws in the barrel is about 5×10^4 [15]. Each straw is divided into two at the centre in order to reduce the occupancy and is read out at each end.

One end-cap part consists of 18 wheels with radial straws. The 14 wheels nearest to the interaction point cover the radial range from 64 to 130 cm. The last four wheels extend to an inner radius of 48 cm. This is necessary to maintain a constant number of crossed straws over the full acceptance. The wheels 7 to 14 have half as many straws per cm in z as the other wheels. The total number of straws in the end-cap part is about 3.2×10^5 [15]. Each straw is readout at the outer radius.

3.2.3 The Calorimeter

The calorimeters measure the energy a particle loses as it passes through the detector. It is usually designed to absorb most of the particles coming from a collision, forcing them to deposit all of their energy within the detector. The incident electrons or photons give rise to an electromagnetic shower that can be described by a cascade of $e^{\pm}$ and γ production (mainly bremsstrahlung and the creation of e^+e^- pairs). The incident hadrons give rise to a hadronic shower consisting of an electromagnetic component ($e^{\pm}$ and γ), a hadronic component of strongly interacting particles and a component of low energetic particles that are not detected. Particle identification is performed using both the electromagnetic and hadronic calorimeters on the basis of transversal and longitudinal shower profiles. The electromagnetic shower gives mainly a signal in the first part of the calorimeter (electromagnetic calorimeter). The hadron gives a signal in both parts of the calorimeter. The design goal energy resolution for photons and electrons is [15]:

$$\frac{\sigma_E}{E} = \frac{0.1}{\sqrt{E}} \oplus 0.01 \oplus \frac{0.3}{E} \tag{3.4}$$

with E in GeV. The design goal energy resolution for hadrons is:

$$\frac{\sigma_E}{E} = \frac{0.5}{\sqrt{E}} \oplus 0.03 \tag{3.5}$$

All calorimeters consist of three parts, a barrel, an end-cap and a forward/backward part as shown in the **Figure 2.18**. The forward/backward calorimeter extends to $|\eta| = 4.9$. This is needed to identify events with missing transverse energy. Both the hadronic and electromagnetic forward calorimeters are liquid argon based and are integrated in the cryostats of the end-cap calorimeters.

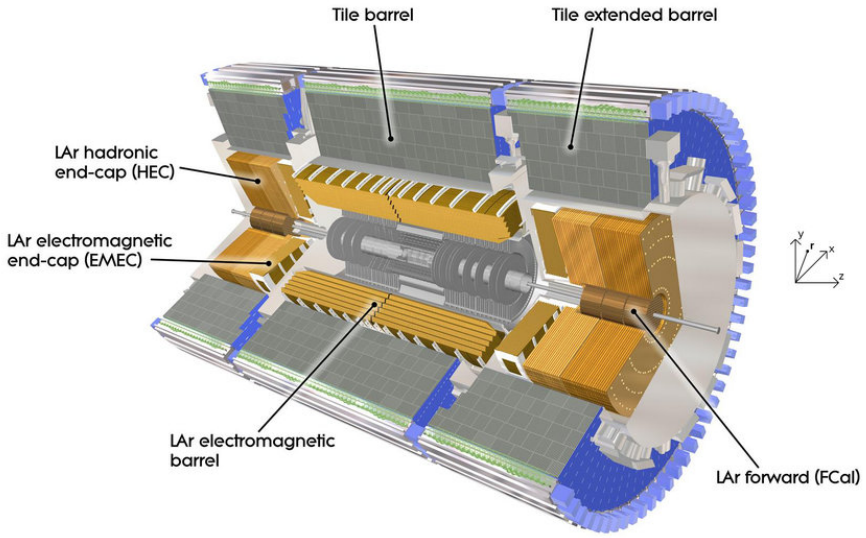

Figure 2.18 A Schematic view of the ATLAS calorimeters.

The barrel and extended barrel region of the hadron calorimetry use iron plates with scintillation plates. In the end-cap-region the hadron calorimeter is based on liquid argon. All electromagnetic calorimetry is based on liquid argon and lead absorbers. The calorimeters are segmented in cells. The electromagnetic calorimeter uses a segmentation varying between $\Delta\eta \times \Delta\phi = 0.003 \times 0.1$ and $\Delta\eta \times \Delta\phi = 0.025 \times 0.025$. The hadronic calorimeter uses a coarser segmentation of $\Delta\eta \times \Delta\phi = 0.1 \times 0.1$ [15].

Other particles than primary muons that are not stopped in the calorimeter give rise to a background signal in the muon spectrometer. The thickness of the electromagnetic calorimeter is about 25-30 radiation lengths. The thickness of the hadronic calorimeter is about 10 absorption lengths.

3.2.4 The Muon Spectrometer

The muon spectrometer is the outermost detector of ATLAS. It is designed to measure high-pT muons with a high precision independent of the inner detector. The spectrometer also provides an independent muon trigger. **Figure 2.19** shows the layout of this spectrometer. It integrates four different detector technologies and the barrel and endcap toroid magnets. The barrel part of the muon spectrometer consists of three concentric layers at radii of about 5 (inner layer), 8 (middle) and 10 (outer) meters. Each layer consist of Monitored Drift Tube (MDT) chambers. The middle and outer layer are in addition equipped with Resistive Plate Chambers (RPC). The MDT chambers provide precision measurements to determine the momentum measurement for both barrel and endcap, except close to the beampipe for the innermost layer of the endcap, where Cathode Strip Chambers (CSC) are positioned.

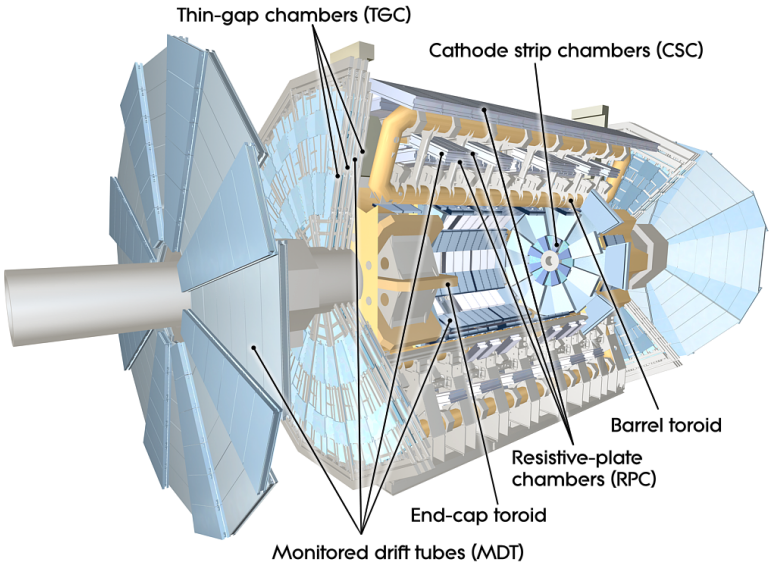

Figure 2.19 A Schematic view of the ATLAS muon system.

The coverage and exact numbers of chambers and channels for the four technologies are given in the **Table 3.2**.

MDT operation

Table 3.2 Detector technologies of the muon spectrometer.

Technology	Function	Coverage	Chambers	Channels
MDT	tracking	$\|\eta\| < 2.7$	1150	354k
CSC	tracking	$2.0 < \|\eta\| < 2.7$	32	30.7k
RPC	trigger	$\|\eta\| < 1.05$	544	373k
TGC	trigger	$1.05 < \|\eta\| < 2.7$	3588	318k

The MDT chambers combine high intrinsic spatial resolution with an internal monitoring system to observe internal deformations of the chamber. They provide for a robust, cost-effective instrumentation suitable for mass production. The basic detection element of an MDT is a cylindrical aluminium drift tube of 30 mm diameter and a central wire of 50 mm diameter at 3270 V with respect to the tube. The detector is operated with a non-flammable gas mixture at 3 bar absolute pressure for reduced diffusion and ionisation fluctuation [15]. There is a linear relation between the drift time and drift distance.

CSC operation

The CSCs are multiwire proportional chambers with wires on a high voltage strung parallel in a gas volume, closed by conducting planes at 0 V. One of the two enclosing planes is appropriately segmented in strips with a readout pitch of 5 mm. The CSCs have a symmetric cell in which the anode-conducting plane distance equals the anode wire spacing. The anode wire spacing has now been fixed at 2.54 mm, which is considerably lower than the tube radius of the MDTs to reduce the occupancy per wire. Precise position measurements along the wires are achieved by determining the centre of gravity of the charge induced on the strips of one of the two conducting planes. With prototypes, resolutions of better than 50 mm have been achieved in test beams [15].

RPC system

A system of the RPCs provide trigger signals in the barrel region. The trigger detector in the barrel is made up of three stations, each with two detection layers.

They are located on both sides of the middle the MDT station, and either directly above or directly below the outer the MDT station. The two stations near the centre provide the low-pT trigger ($pT > 6$ GeV). The third station, at the outer radius of the magnet, allows to increase the pT threshold to 20 GeV, for the high-pT trigger. The RPC is a gaseous parallel-plate detector with a typical spatial resolution of the order of 1 cm and a typical time resolution of the order of 1 ns [15].

TGC system

The TGCs provide trigger capabilities in the end-cap region. Seven layers of TGCs complement the middle the MDT station. Two layers of the TGCs complement the inner the MDT station.The TGCs are standard multiwire proportional chambers, but with small anode-to-anode, (wire-to-wire) distance (1.8 mm) and small cathode-to-anode distance (1.4 mm) [15]. The spatial and time resolution of the TGCs is similar to the RPCs.

3.2.5 The Magnet System

The magnet system of the ATLAS detector consists of four superconducting magnets:

- A central solenoid
- An air-core barrel toroid
- Two air-core end-cap toroids

A three-dimensional view of the bare windings of the ATLAS magnet system is given in **Figure 2.20**. In principle the three toroidal magnets could have been combined into a single large toroidal magnet. For technical reasons the toroidal system is split into three subsystems.

Toroid magnets

Each toroid consists of eight coils with 120 (barrel) or 116 (end-cap) turns. As all coils are superconducting, cooling circuits, a vacuum system and cryostats for

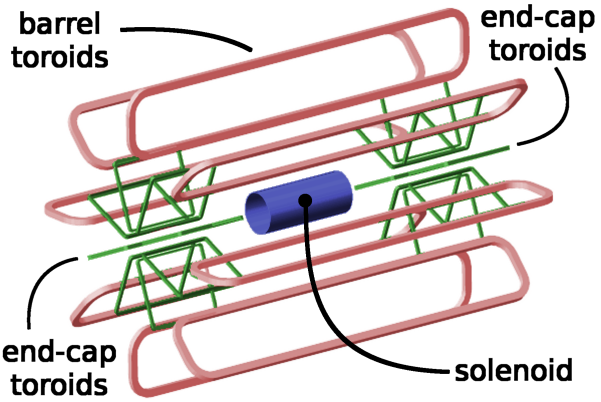

Figure 2.20 A three-dimensional view of the bare windings of the ATLAS magnet system [16].

optimum thermal insulation of the coils are required. Each coil has an operation temperature of 4.5 K and is enclosed by a cryostat [15]. The Lorentz forces between the coils and the weight of the coils require additional mechanical structures between the coils. The toroid magnets generate a toroidal magnetic field configuration for the muon spectrometer. The advantage of a toroidal magnetic field is that its direction is almost perpendicular to the direction of flight of the particles.

Central solenoid

The central solenoid consists of one coil with 1173 turns. The central solenoid is designed to provide for the inner detector an axial magnetic field of 2 T. Its axis coincides with the beam axis. The axial length of the solenoid is 5.3 m. The magnetic field points in the positive z-direction.

Field integrals

The most important numbers for track momentum measurements are the field integrals over the track length inside the tracking volume [15]:

$$\begin{aligned} I_1 &= \int B sin\theta_{d\vec{l}\vec{B}} dl \\ I_2 &= \int \int B sin\theta_{d\vec{l}\vec{B}} dl dr \end{aligned} \tag{3.6}$$

with $tan\theta$ the slope in the (r, z) plane. I_1 is the integral of Bdl as a measurement of the bending power of the field. I_2 is the double integral of the field that is

especially important for momentum measurements. The toroidal magnetic field provides for typical bending powers of 3 Tm in the barrel and 6 Tm in the end-cap regions. The solenoidal magnetic field provides for a typical bending power of 2.1 Tm. The tracking capacity of the ATLAS solenoid has been compared with the tracking capacity of an ideal solenoid field. The degradation in the tracking capacity in the high rapidity region ($1.6 < |\eta| < 3.2$) is at most 10% [15].

Chapter 4

Measurement of the $t\bar{t}\gamma\gamma$ Production Cross Section

This Chapter describes the measurement of the $t\bar{t}\gamma\gamma$ production cross-section in proton-proton collisions at a center-of-mass-energy of $\sqrt{s} = 13$ TeV corresponding total integrated luminosity of 36.1 fb^{-1} with the ATLAS detector in the single lepton channels. The final state of the $t\bar{t}\gamma\gamma$ process is similar to the $t\bar{t}\gamma$ process, but it contains two prompt photons. So, this analysis is built on the single-lepton $t\bar{t}\gamma$ analysis[17] in ATLAS. The event yields and kinematic distributions are compared between data and MC in the signal region.

The sections of this chapter are structured as follows: Firstly, the data and object definitions are introduced. The event selection for the single-lepton $t\bar{t}\gamma\gamma$ final state is described in the Section 4.3. Then, the kinematic distributions are compared between data and MC after applying the selections. Further, the background descriptions are discussed in Section 4.5. Finally, the description of the fiducial cross section measurement and the estimations of the systematic uncertainties are presented.

4.1 Data and Simulation samples

This analysis has been performed with proton-proton collision data collected by the ATLAS detector during 2015 and 2016, at a center-of-mass-energy of $\sqrt{s} = 13$ TeV. The corresponding total integrated luminosity is 3.21 fb^{-1} in 2015 and 32.88 fb^{-1} in 2016, respectively.

The signal sample is the $t\bar{t}\gamma$ sample which has been simulated for single lepton and dilepton channels of $t\bar{t}$ at leading-order, with the MG5-aMC@NLO generator [17], using the NNPDF2.3LO parton distribution function [17]. The showering and hadronisation is done by Pythia8, i.e. interfaced to the Pythia8. The first photon of the $t\bar{t}\gamma\gamma$ process is simulated from the matrix element and the second photon by the parton shower which the second photon is selected using a truth matching in this $t\bar{t}\gamma$ sample. The production of W- and Z-bosons with an associated prompt photon as well as the other vector boson production samples (W and Z-bosons + jets) are simulated using SHERPA 2.2.2 and 2.2.1, respectively, with the NNPDF30NNLO pdf set [17]. Also for the $W\gamma\gamma$ and $Z\gamma\gamma$ processes the second photon is selected using the truth matching in the $W\gamma$ and $Z\gamma$ samples. The MC sample for the inclusive $t\bar{t}$ production is generated with POWHEG-BOX v2 interfaced to PYTHIA8, using the A14 tune [17]. The $t\bar{t}$, W+jets and Z+jets samples can contain events already taking into account by the $t\bar{t}\gamma$, $W\gamma$, $Z\gamma$ samples due to the photon by the showering. This overlap is removed using the truth matching. The single top-quark t-, s- and Wt-channel samples are produced by POWHEG-Box v1 generator. The WW-, WZ- and ZZ-diboson samples are simulated using SHERPA 2.1 with the CT10(NLO) pdf set [17]. For the single top+$\gamma\gamma$ and diboson+$\gamma\gamma$ processes two photons are simulated by the parton shower which both photons are selected using the truth matching in the single top+γ and diboson+γ samples. The $t\bar{t}H$ sample is simulated with the MG5-aMC@NLO generator, using the NNPDF2.3LO parton distribution function. In the $t\bar{t}H$ process the Higgs decay to two photons. There is also the $t\bar{t}\gamma\gamma$ signal sample. But in this analysis this sample is not used because of the limiting factor (e.g k-factor) in this sample.

All simulation samples which are the $t\bar{t}\gamma$, $t\bar{t}$, single top-quark, diboson, Wγ, Zγ, W+jets, Z+jets and $t\bar{t}H$ are normalized to the data luminosity. They are used to

evaluate a signal acceptance, a correction factor as well as background estimation in the $t\bar{t}\gamma\gamma$ process.

4.2 Object Definitions

The single-lepton $t\bar{t}\gamma\gamma$ final state consists of the following objects: leptons (e^- or μ), jets, b-jets, missing transverse energy and photons. The object definitions based on the $t\bar{t}\gamma$ analysis are applied in this analysis. The definitions are chosen to be as close as possible to the ones of the usual $t\bar{t}$ analysis.

4.2.1 Object Selections

Electrons

The electrons are built from energy deposits in the the Electromagnetic Calorimeter associated with tracks from the Inner Detector. The candidates have to satisfy:

- TightLH identification criteria,
- Gradient isolation criteria,

and they are required to have a transverse momentum of $p_T > 25$ GeV and $|\eta_{clus}| < 2.47$ (η_{clus} is the pseudo rapidity of the calorimeter cluster associated to the electron), excluding the transition region between barrel and endcap EM calorimeters, $1.37 < |\eta_{clus}| < 1.52$. The reconstruction, identification and scale factor extraction methods, the isolation and the calibration is described in [17].

Muons

The muon candidates are identified by matching tracks in the muon spectrometer with tracks in the Inner Detector. They are required to have:

- Medium identification quality criteria,
- Gradient isolation criteria.

Only muons with calibrated $p_T > 25$ GeV and $|\eta_{clus}| < 2.5$ are considered.

Photons

The photons are reconstructed from energy deposits in the Electromagnetic Calorimeter. The reconstructed photons are classified into the converted and unconverted photons depending on if the cluster is matched or not matched to any reconstructed tracks in the Inner Detector. The photons have to satisfy:

- Tight identification criteria,
- to be isolated, using the FixedCutTight.

The candidates are considered to have a transverse momentum of $p_T > 20$ GeV and $|\eta_{clus}| < 2.37$ ($|\eta_{clus}|$ is the pseudo-rapidity of the calorimeter cluster associated to the photon), excluding the crack region $1.37 < |\eta_{clus}| < 1.52$.

Jets

The jets are reconstructed using the anti-k_t algorithm with a radius parameter $R = 0.4$ and are reconstructed from topological calorimeter clusters. The candidates with a transverse momentum of $p_T > 25$ GeV and $|\eta| < 2.5$ are considered [17].

To suppress jets from pile-up, jets are required to have a Jet Vertex Tagger discriminant larger than 0.59 for jets with a transverse momentum of $p_T < 60$ GeV and $|\eta| < 2.4$.

b-jets

The jets containing b-hadrons are tagged by an algorithm. The MV2c10 algorithm which is based on a boosted decision tree, identifies the jets from b-quark hadronisation which working point of b-tagging is used.

Missing transverse energy

The missing transverse energy, E_T^{miss} originating from the neutrino in the leptonic decay of a W boson is calculated as the negative vector sum of the transverse momentum of all topoclusters in the event.

Overlap removal

To avoid the same deposit in the calorimeters or track being used to reconstruct two different objects, the following overlap removal procedure is used:

- Firstly electrons that are sharing their track with a muon candidate are removed.
- Then, all the jets that are close to an electron in the $\eta - \phi$ plane ($\Delta R < 0.2$) are removed.
- Then, all the electrons that are close ($\Delta R < 0.4$) to a remaining jet are removed.
- For muons and jets that are close ($\Delta R < 0.4$), the muon is removed if the jet has more than two associated tracks, otherwise the jet is removed.
- All the photons that are close ($\Delta R < 0.4$) to a remaining electron or muon are removed.
- Finally, all the jets that are close ($\Delta R < 0.4$) to a remaining photon are removed.

4.3 Event Selection

In the single lepton channels, the $t\bar{t}\gamma\gamma$ final state contains two isolated photons with high-p_T, an isolated lepton (e^- or μ) with a large p_T, large missing transverse momentum originating from the neutrino in the leptonic decay of a W boson, two jets from the hadronic decay of the other W boson, and two b-quark jets.
The following selection based on the object definitions is applied to select the single-lepton $t\bar{t}\gamma\gamma$ events. The selection is similar to the selections which are used in the $t\bar{t}\gamma$ final state [17], but one additional prompt photon is selected.

For e+jets (μ+jets) channels:

- Exactly one electron (muon) with $p_T > 25$ GeV is required.
- Exactly two reconstructed photons satisfying the Tight identification criteria and being isolated are required with $p_T > 20$ GeV and $|\eta_{clus}| < 2.37$.
- At least four reconstructed jets with $p_T > 25$ are required,
- At least one jet has to be b-tagged jet.
- For e+jets channel: An invariant mass $m(\gamma, e)$ between each prompt photon and electron has to be outside a 5 GeV mass window around the Z boson mass.
- Distance between each prompt photon and the lepton must be greater than 1.0.

This is to limit the contribution from the photons originating from top decay products in the radiative top decay process.

- Event double counting removal: To avoid a double counting with the W$\gamma\gamma$, Z$\gamma\gamma$, $t\bar{t}\gamma\gamma$, the events with two prompt photons in the W+jets, Z+jets and $t\bar{t}$ MC samples are removed by using the truth matching which identifies the origin and the type of the truth particle corresponding to the reconstructed photon.

The following table shows the summary of the event selection for single lepton channels.

Table 3.4 Summary of the event selections.

Channel	e+jets	μ+jets
Lepton	1 e	1 μ
Photon	2γ with $E_T > 20$ GeV	
Jet	≥ 4	
b-jet	≥ 1	
$m(\gamma, e)$	not in [85,95] GeV	-
$\Delta R(\gamma, l)$	≥ 1	

In the **Table 3.5** the events passing above selection are shown. Full cutflows are given in the Appendix A. Selection yields a total of 28 ± 5.29 and 17 ± 4.12 data events with statistical errors in the electron and muon channels, respectively. From simulation studies with the $t\bar{t}\gamma\gamma$ signal sample, 11.15 ± 0.75 and 12.52 ± 0.84 signal events with statistical errors are predicted in the electron and muon channels, respectively. Those predicted events are normalized to the total integrated luminosity of 36.1 fb^{-1} and weighted with the pile-up, MC weight and scale factors per photon, lepton, jet, btag. Also the k-factor for signal sample which is a ratio of cross sections between the NLO theory and the LO MadGraph in the same phase space used for theory calculation [17] is applied.

Table 3.5 The event yields for each sample and e+jets(μ+jets) channel. Only statistical uncertainties are included.

Process	e+jets	μ+jets
$t\bar{t}\gamma\gamma$	11.15 ± 0.75	12.52 ± 0.84
W$\gamma\gamma$	0 ± 0	0.37 ± 0.37
Z$\gamma\gamma$	0.60 ± 0.60	0.57 ± 0.36
Single top+$\gamma\gamma$	0 ± 0	0 ± 0
Diboson+$\gamma\gamma$	0 ± 0	0 ± 0
$t\bar{t}$H	1.41 ± 0.17	1.04 ± 0.15
Fake Photon	3.82 ± 0.51	2.31 ± 0.66
Fake Lepton	1.10 ± 2.58	0 ± 0.84
Total	18.08 ± 2.80	16.81 ± 1.46
Data	28 ± 5.29	17 ± 4.12

In the **Table 3.5** the events corresponding to the fake photons are sum of the events with two hadronic fakes, two electron fakes, one fake and one prompt photon, and one electron fake and hadron fake. These events are selected in the $t\bar{t}$, V+jets and $V\gamma$ simulation samples. In the $t\bar{t}$, V+jets processes the double counting removal which removes the events with two prompt photons is applied. This removal procedure is done by using the truth matching which identifies the origin and the type of the truth particle corresponding to the reconstructed photon. Because the showering procedure will add photon radiations, the $t\bar{t}$ and V+jets samples can contain events already taking into account by the $t\bar{t}\gamma$ and Vγ samples. Further, in the fake photon background study, it will be explained in detail. The fake lepton events correspond to the events with non-prompt lepton and the QCD multijets evets with the photon production. For other processes the events with additional two prompt photons are selected using the selection as described in 4.3. These events contirbute to the prompt photon background.

4.4 Kinematic Distributions

In this Section the following kinematic distributions are compared between data and MC:

- The invariant mass distribution of two prompt photons,
- The transverse momentum distributions of the electron, muon, first photon, second photon and jets,
- The pseudo-rapidity distributions of the electron, muon, first photon, second photon and jets,
- The distributions of the distance between lepton and each prompt photons, $\Delta R(l, \gamma)$,
- The distributions of the invariant mass between electron and each prompt photons, $m(e, \gamma)$

All distributions for e+jets and μ+jets channels are plotted in the signal region.

The **Figure 2.21** shows the distributions of the transverse momentum of the first and second prompt photon with $p_T > 20$ GeV in the e+jets and μ+jets channel, respectively. The electron, muon and jets transverse momentum distributions are included in the Appendix B.

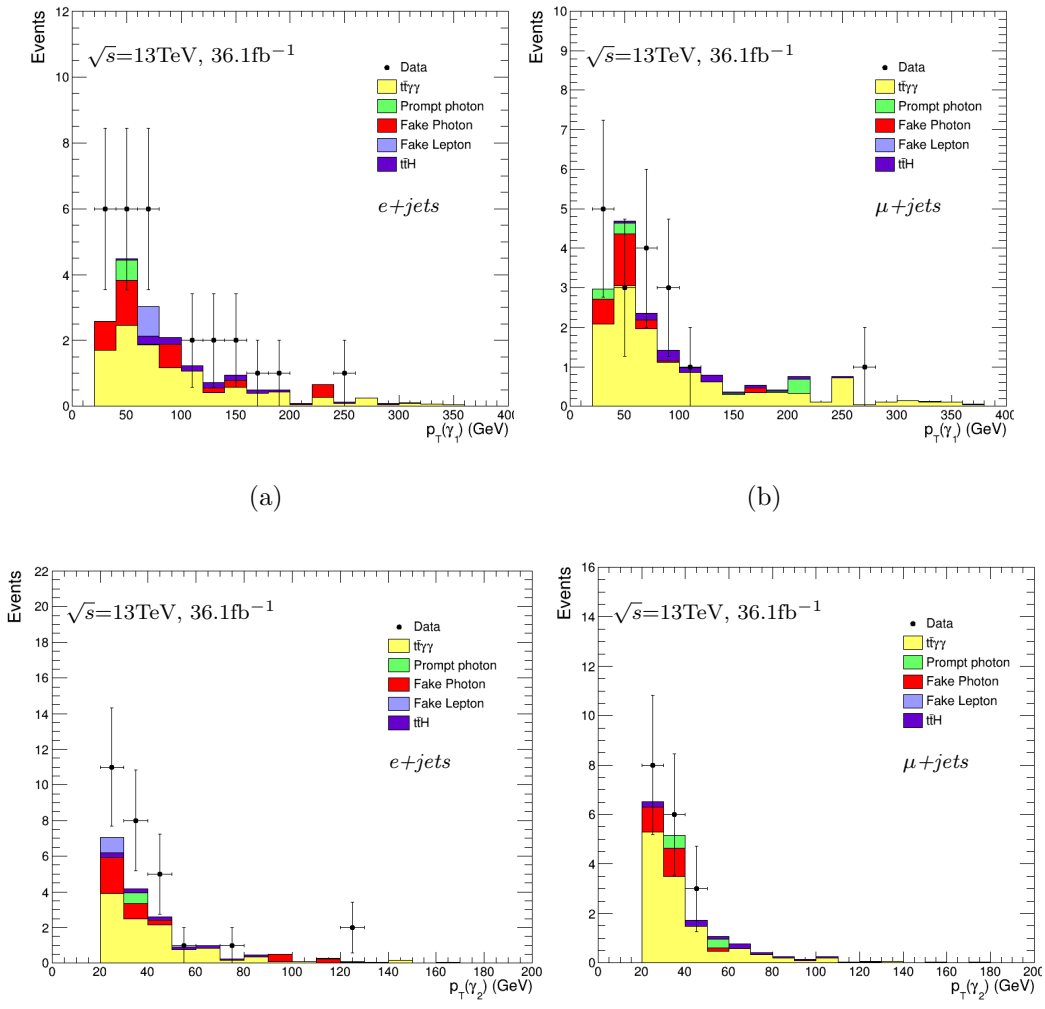

Figure 2.21 The distributions of the transverse momentum of the first and second prompt photon. The left two plots correspond to the distributions in the e+jets channel, the right two plots in the μ+jets channel, respectively.

The **Figure 2.22** shows the distributions of the first and second prompt photon pseudo-rapidity with $|\eta_{clus}| < 2.37$ in the e+jets and μ+jets channel, respectively. The electron, muon and jets pseudo-rapidity distributions are included in the Appendix B.

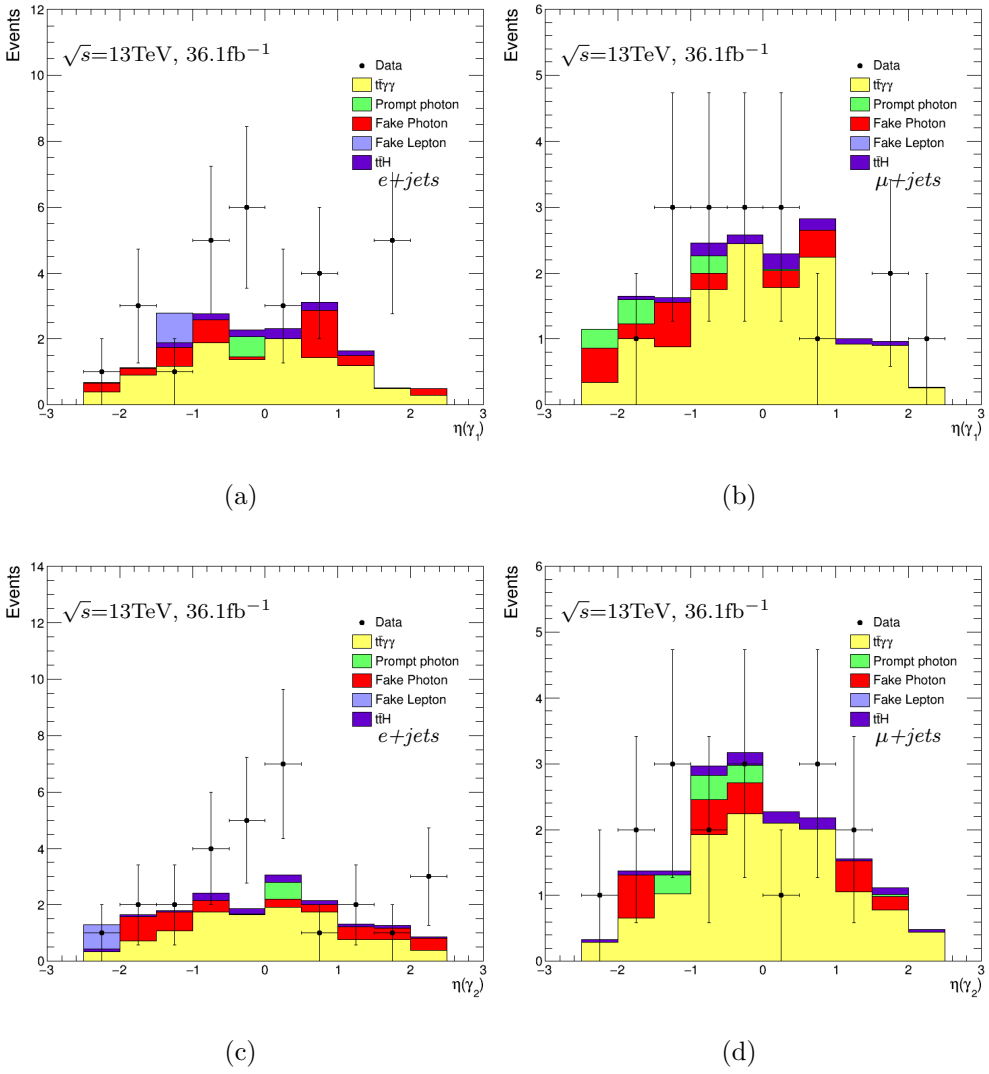

Figure 2.22 The distributions of the pseudo-rapidity of the first and second prompt photon. The left two plots correspond to the e+jets channel, the right two plots to the μ+jets channel, respectively.

The invariant mass distributions of two prompt photons are shown in the **Figure 2.23**. The invariant mass of two prompt photons are calculated using the energy and momentum of each prompt photon. This is done by a general four vector class in ROOT[18].

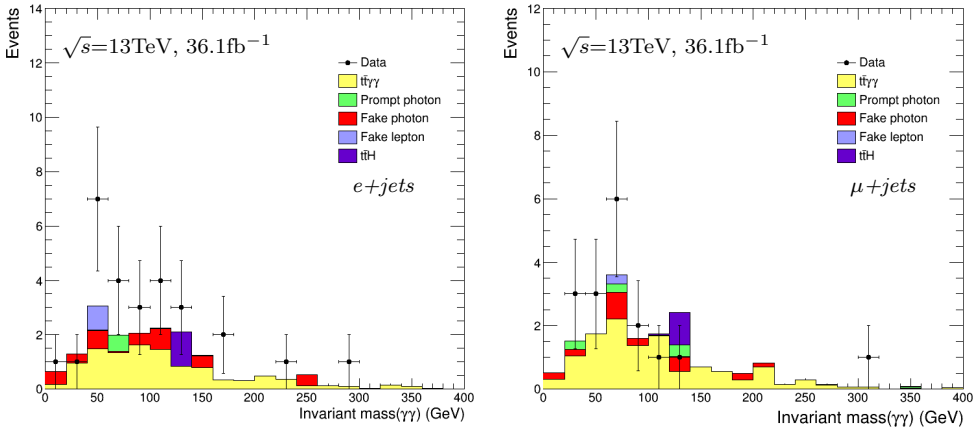

(a) (b)

Figure 2.23 The two prompt photons invariant mass distributions. The left plot corresponds to the distribution in the e+jets channel, and the right plot in the μ+jets channel, respectively.

The distributions of the invariant mass between electron and each prompt photon being outside a 5 GeV mass window of the Z mass are shown in the **Figure 2.24**

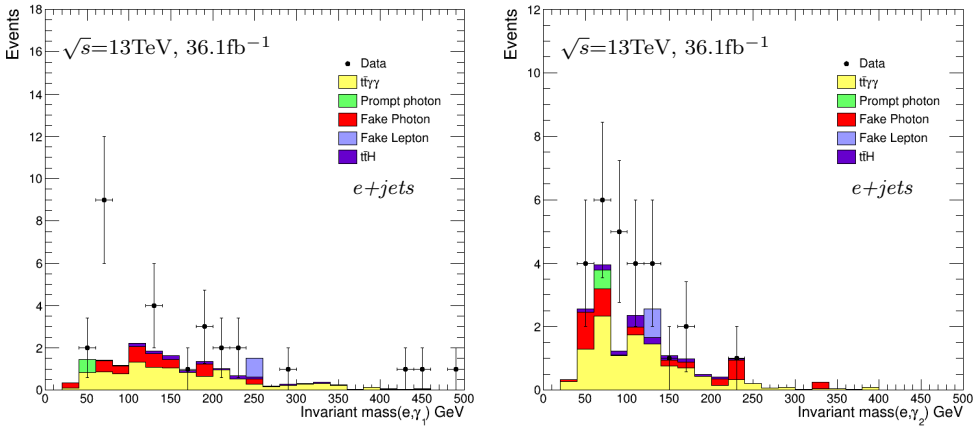

(a) (b)

Figure 2.24 The electron and each prompt photon invariant mass distributions in the e+jets channel.

In this analysis, the distance between lepton and each prompt photon $\Delta R(l, \gamma)$ is considered to be greater than 1.0. This is to limit the contribution from the photons originating from top decay products in the radiative top decay process. In the **Figure 2.25** the distance between electron and each prompt photon $\Delta R(e, \gamma)$, and the distance between muon and each prompt photon $\Delta R(\mu, \gamma)$ distributions are shown in the e+jets and μ+jets channel, respectively.

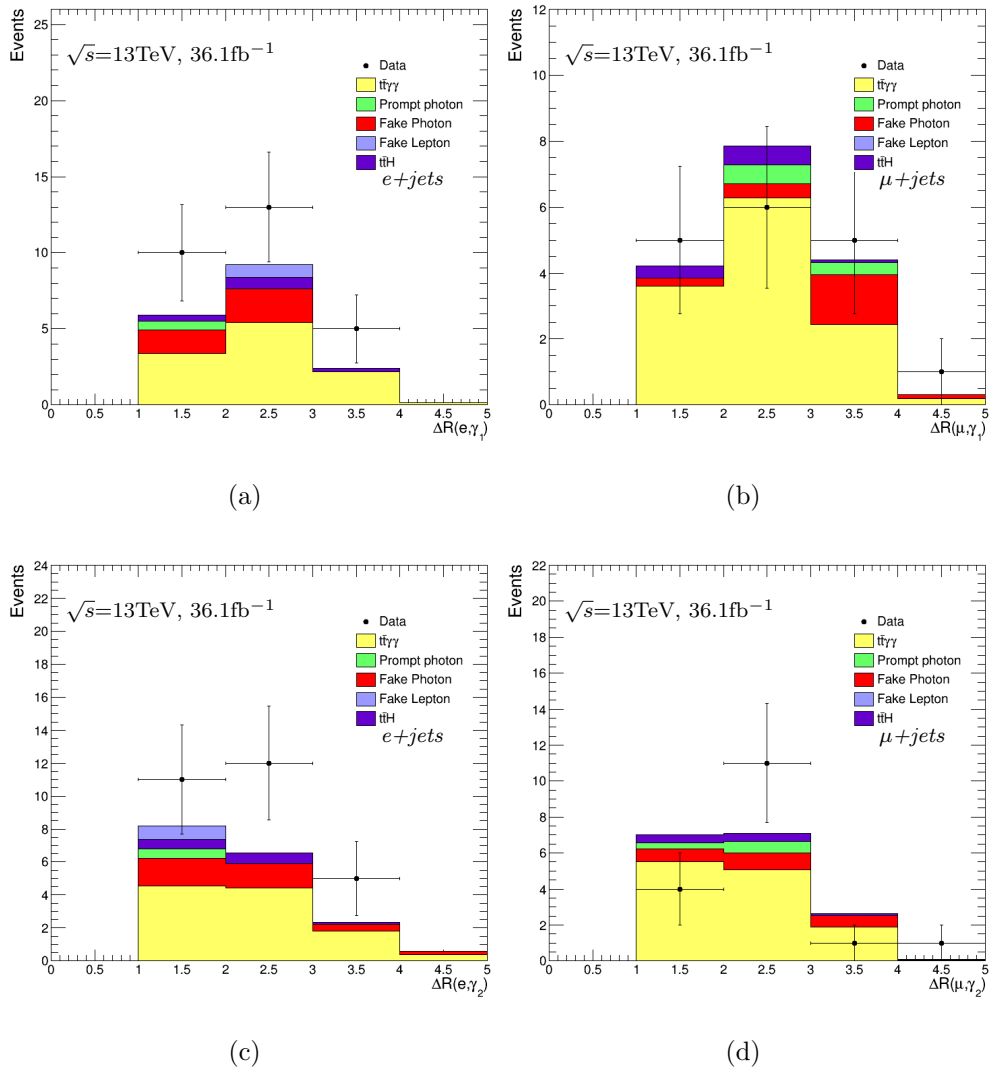

Figure 2.25 The distributions of the distance between lepton and each prompt photon. The left two plots correspond to the e+jets channel, the right two plots to the μ+jets channel, respectively.

Finally, in the **Figure 2.26** the $\Delta R(l,\gamma)$ distributions are plotted before and after applying the mass window cut and $\Delta R(l,\gamma) > 1.0$ cut in the e+jets and μ+jets channel, respectively. These plots are plotted using only signal sample.

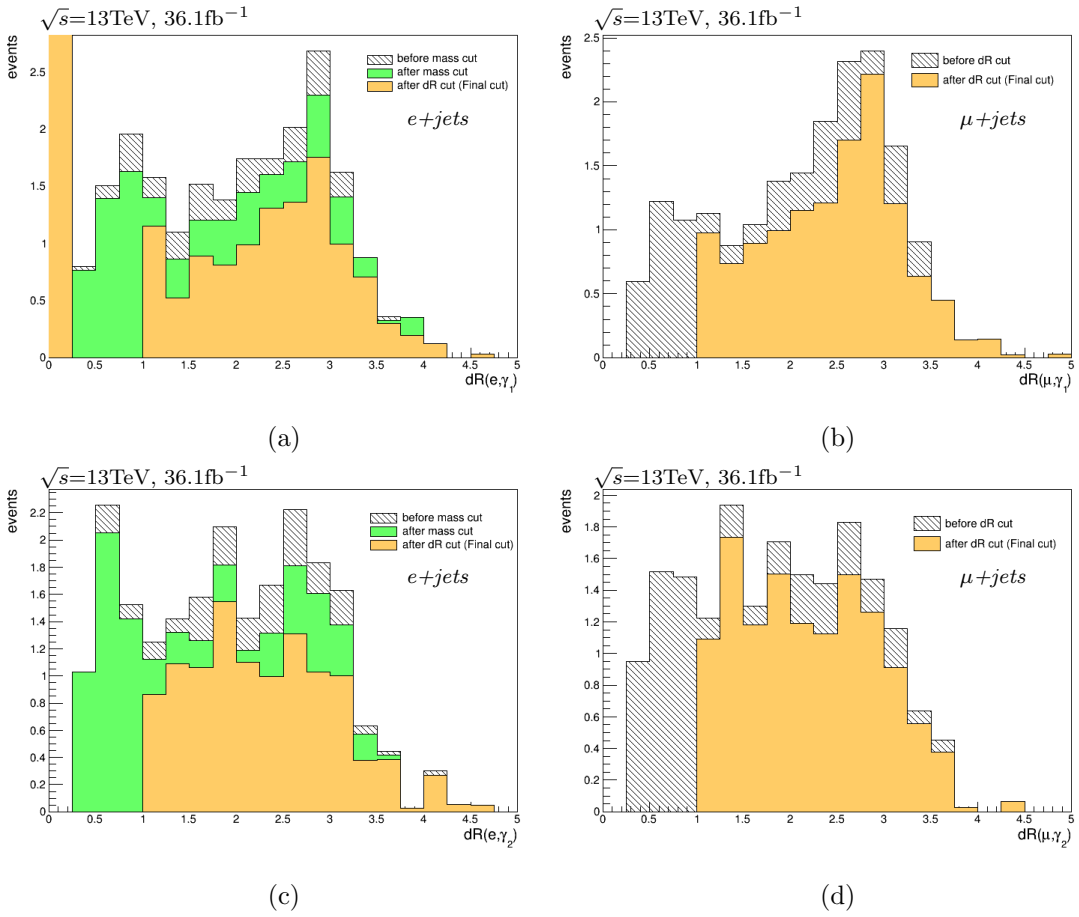

Figure 2.26 The $\Delta R(l,\gamma)$ distributions before and after applying the mass window cut and $\Delta R(l,\gamma) > 1.0$ cut in the e+jets and μ+jets channels, respectively.

Other kinematic distributions are included in the Appendix B.

4.5 Background Descriptions

There are several background contributions which come from events with prompt photon, fake photon and fake lepton in this analysis. One of the largest background contribution to the $t\bar{t}\gamma\gamma$ process is from events with the fake photons. This contribution is categorized as follows:

- Two hadronic fakes background (HFake) ,
- Two electron fakes background (EFake),
- One fake and one prompt photon background, - One hadronic fake and one electron fake background

The contribution of the two hadronic fakes background comes from events with the two photons coming from hadron decay. Similarly, the contribution from events with the two electron fakes comes from events with electrons misidentified as photons. Also, the first photon can be originating from hadron decay and the second photon coming from electron fakes. In this case this contribution is included in the one hadronic fake and one electron fake background. In the Section 4.5.3 the fake photon background is described more in detail.

The contributions of the fake lepton or QCD background which comes from the fake leptons, and the prompt photon background which is from non-$t\bar{t}$ events with two prompt photons are introduced in this Chapter.

4.5.1 Fake Photon Backgrounds

Two hadronic fakes background

One of the important background contributions to the $t\bar{t}\gamma\gamma$ process is the two hadronic fakes which comes from hadrons, or the photons originating from hadron decay that are misidentified as the prompt photons. This background is estimated from MC simulation samples. The events with two hadronic fakes are selected using the selection as described in Section 4.3, with truth matching which identifies the origin and type of the truth particle corresponding to the reconstructed photon. Using the truth matching the events with two prompt photons are removed in the

W+jets, Z+jets, and $t\bar{t}$ productions. **Figure 2.27** the contributions of the two hadronic fakes background are summarized in the e+jets and μ+jets channels, respectively. The dominant contribution to this background comes from the $t\bar{t}$ production with two hadronic fakes. Also the W+jets events with two hadronic fakes in the e+jets channel contributes to this background.

Two electron fakes background

In the two electron fakes background the electrons are misidentified as photons. The contribution to the this background comes from the $t\bar{t}$ events both top quarks decaying semileptonically and from the W+jets and Z+jets productions. This background is estimated from MC simulation. The events with two electronic fakes are selected using selection as described in Section 4.3, with the truth matching based on PdgId of the matched MC photon and the distance between the reconstructed photon and the closest truth electron. This is summarized in the **Figure 2.27**. In this analysis there is no two electron fakes contribution to the $t\bar{t}\gamma\gamma$ process.

One hadronic fake and one electron fake background

Since each photon has three types which are the hadronic, electron and prompt photon, two photons in the fake photon background can be eight possible combinations of their types. In this background the contribution coming from events with one photon originating from hadron decay and another one photon misidentified as electrons are considered. These events with one hadronic fake and one electron fake are the one of the dominant background contributions to the $t\bar{t}\gamma\gamma$ process. These events are selected by applying the selection as described in Section 4.3, with the truth matching in the e+jets and μ+jets channels, respectively. **Table 3.6** summarizes this background contributions to the $t\bar{t}\gamma\gamma$ process with only statistical uncertainty. The contributions from events with two hadronic fakes or two electron fakes are not included in this background.

One fake photon and one prompt photon background

As mentioned previously, two photons in the fake photon background can be eight possible combinations of their types. One of these combinations is that one photon can be originating from hadron decay and another one being a prompt photon. In this case this contribution is included in this background. This background is the one of the largest background contributions to the $t\bar{t}\gamma\gamma$ process. The events with one fake photon and one prompt photon are selected by applying the selection as described in Section 4.3, with the truth matching in the e+jets and μ+jets channels, respectively. In the **Table 3.6** this background contributions are summarized. The largest contribution to this background is from events with one prompt photon and one electron fake of the $t\bar{t}$ and Z+jets processes in the e+jets channel. The second dominant contribution comes from events contain one prompt photon and one hadronic fake of the $t\bar{t}$ process in the μ+jets channel. The contributions from events with two hadronic fakes or two electron fakes are not included in this background.

Table 3.6 The events with one fake photon and one prompt photon, and the events with one hadronic fake and one electron fake are shown with only statistical errors in the the e+jets and μ+jets channels, respectively. The numbers are normalized to the total integrated luminosity of 36.1 fb^{-1}.

Process	Photon types	e+jets	μ+jets
W+jets	Prompt(γ_1) & HF(γ_2)	0 ± 0.04	0 ± 0
	Prompt(γ_1) & EF(γ_2)	0 ± 0.04	0 ± 0
	HF(γ_1) & Prompt(γ_2)	0 ± 0.04	0 ± 0
	EF(γ_1) & Prompt(γ_2)	0 ± 0	0 ± 0
	EF(γ_1) & HF(γ_2)	0 ± 0	0 ± 0
	HF(γ_1) & EF(γ_2)	0 ± 0	0 ± 0
Z+jets	Prompt(γ_1) & HF(γ_2)	0 ± 0	0 ± 0
	Prompt(γ_1) & EF(γ_2)	0.12 ± 0.001	0 ± 0
	HF(γ_1) & Prompt(γ_2)	0.004 ± 0.001	0 ± 0
	EF(γ_1) & Prompt(γ_2)	0.1 ± 0.05	0 ± 0
	EF(γ_1) & HF(γ_2)	0 ± 0	0 ± 0
	HF(γ_1) & EF(γ_2)	0 ± 0	0 ± 0
$t\bar{t}$	Prompt(γ_1) & HF(γ_2)	0.44 ± 0.06	0 ± 0.16
	Prompt(γ_1) & EF(γ_2)	1.66 ± 0.06	0.43 ± 0.16
	HF(γ_1) & Prompt(γ_2)	0.24 ± 0.06	0.47 ± 0.16
	EF(γ_1) & Prompt(γ_2)	0.73 ± 0.37	0.99 ± 0.45
	EF(γ_1) & HF(γ_2)	0 ± 0	0 ± 0
	HF(γ_1) & EF(γ_2)	0 ± 0	0 ± 0
$V\gamma\gamma$	Prompt(γ_1) & HF(γ_2)	0 ± 0	0 ± 0
	Prompt(γ_1) & EF(γ_2)	1.66 ± 0.06	0 ± 0
	HF(γ_1) & Prompt(γ_2)	0 ± 0	0 ± 0
	EF(γ_1) & Prompt(γ_2)	0 ± 0	0 ± 0
	EF(γ_1) & HF(γ_2)	0 ± 0	0 ± 0
	HF(γ_1) & EF(γ_2)	0 ± 0	0 ± 0

The **Figure 2.27** shows the summary of the contributions coming from events with at least one fake photon in the $t\bar{t}$, V+jets and V+$\gamma\gamma$ processes. In the **Figure 2.27** the types of the first photon are shown along x-axis and the second photon types, y-axis, respectively. For instance, the first box in the each process is removed. Because the events with two prompt photons are removed using the truth matching.

The two hadronic fakes background, and one fake and one prompt photon background in the $t\bar{t}$ process give the largest contributions to the fake photon background. Also the second dominant contribution comes from the two hadronic fakes background and one fake and one prompt photon background in the Z+jets process.

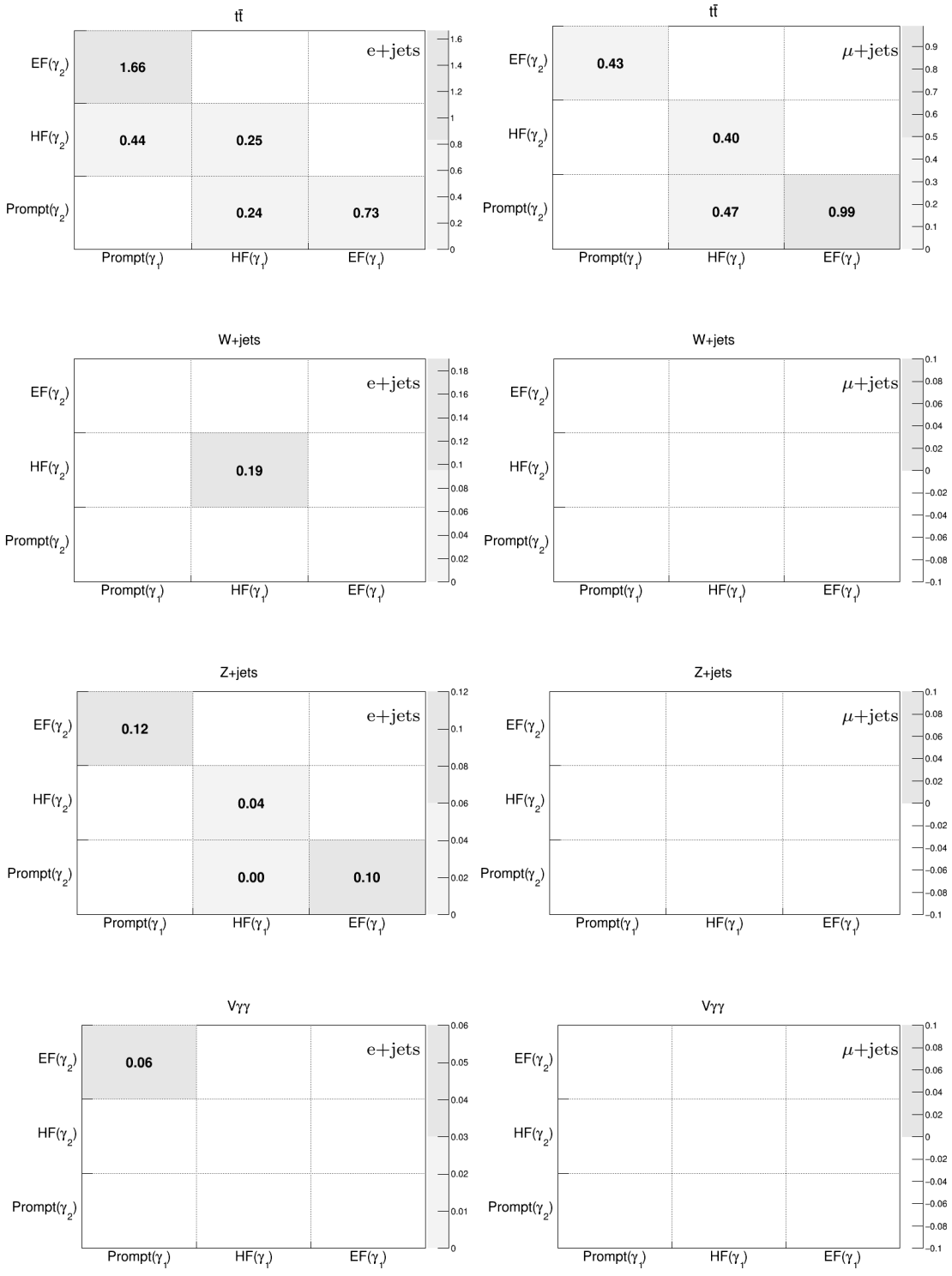

Figure 2.27 The events contain two photons which have three different types of the hadronic fake(HF), electron fake(EF) and prompt photon in the $t\bar{t}$, V+jets and V+$\gamma\gamma$ processes. Left plots correspond to the e+jets channel, the right plots to the μ+jets channel, respectively.

4.5.2 Prompt Photon Background

The contribution to the prompt photon background comes from non-$t\bar{t}$ events with additional two prompt photons. This background is estimated from MC simulation. The W$\gamma\gamma$, Z$\gamma\gamma$, Single Top+$\gamma\gamma$, Diboson+$\gamma\gamma$ and $t\bar{t}H$ processes give the dominant contribution to this background. The events with two prompt photons are selected using the single-lepton $t\bar{t}\gamma\gamma$ selection with the truth matching which identifies the origin and the type of the truth particle corresponding to the reconstructed photon. The **Table 3.7** summarizes the prompt photon background events in the e+jets and μ+jets channel, respectively.The largest contribution comes from the $t\bar{t}H$ process. The dominant contributions to this background come from events of the Z$\gamma\gamma$ production in the e+jets channel and W$\gamma\gamma$ production in the mu+jets channel, respectively.

Table 3.7 The prompt photon background events in the e+jets and μ+jets channels, respectively. The numbers are normalized to the total integrated luminosity of 36.1 fb^{-1}. Only statistical uncertainties are included.

Process	e+jets	μ+jets
W$\gamma\gamma$	0 ± 0	0.37 ± 0.37
Z$\gamma\gamma$	0.60 ± 0.60	0.57 ± 0.36
Single top+$\gamma\gamma$	0 ± 0	0 ± 0
Diboson+$\gamma\gamma$	0 ± 0	0 ± 0
$t\bar{t}H$	1.41 ± 0.17	1.04 ± 0.15

4.5.3 Fake Lepton Background

Another important contribution to the $t\bar{t}\gamma\gamma$ process comes from fake leptons. They are the non-prompt leptons misidentified as prompt leptons coming from the decay of a heavy hadron (bottom or charm hadrons) or they can be produced from the decay of a pion or a kaon. In the single lepton channel the contribution of this

background is typically from QCD multijets events with photons production. The fake lepton events are selected using the same selection as the $t\bar{t}\gamma\gamma$ selection, but the photon truth matching is not applied. In addition, to estimate the fake lepton background the matrix method based on classifying leptons into loose and tight is used. The loose and tight definitions are as follow:

- Tight definition:
For electrons: Tight LH, $p_T > 25$ GeV and gradient isolation.
For muons: Medium ID, $p_T > 25$ GeV and gradient isolation.

- Loose definition:
For electrons: Medium LH and no isolation.
For muons: Medium ID and no isolation

In the Table 3.8 the fake lepton background events are summarized in the e+jets and mu+jets channel, respectively.

Table 3.8 The fake lepton background events in the e+jets and μ+jets channel, respectively. The numbers are normalized to the total integrated luminosity of 36.1 fb^{-1}. Only statistical uncertainties are included.

Process	e+jets	μ+jets
Lep fakes	1.10 ± 2.58	0 ± 0.84

In the **Table 3.9** all background contributions to the $t\bar{t}\gamma\gamma$ process are summarized in the e+jets and μ+jets channel, respectively.

Table 3.9 All background contributions to the $t\bar{t}\gamma\gamma$ process in the e+jets and μ+jets channel, respectively. The numbers are normalized to the total integrated luminosity of 36.1 fb^{-1}. Only statistical uncertainties are included.

Process	e+jets	μ+jets
Hadronic fakes	0.48 ± 0.31	0.42 ± 0.40
Electron fakes	0 ± 0	0 ± 0
Event with at least one fake	3.34 ± 0.40	1.89 ± 0.53
Prompt Photon	0.60 ± 0.60	0.94 ± 0.52
Fake Lepton	1.10 ± 2.58	0 ± 0.84
$t\bar{t}H$	1.41 ± 0.17	1.04 ± 0.15

4.6 Cross section definitions

This section introduces the fiducial cross section measurement of the $t\bar{t}\gamma\gamma$ production. The signal acceptance and correction factors which are needed for a fiducial cross section expression are presented in the Section 4.6.1.

The fiducial cross section measurement is performed in the fiducial region which is defined for MC events at particle level using the object definitions and event selections and is defined to mimic those at the reconstruction level. In this analysis, there are two fiducial regions corresponding to the e+jets and μ+jets channels.

• Particle definitions for fiducial region

Leptons:

Exactly one good lepton is required to have $p_T > 25$GeV and $|\eta| < 2.5$ and not from hadron decay.

Jets:

Good jets are required to have $p_T > 25$GeV and $|\eta| < 2.5$.

b-jets:

Flavour of the jet is determined by ghost matching.

Photons:

Two good photons are required to have $E_T > 20$GeV and $|\eta| < 2.37$.

• **Event selection for fiducial region**

Leptons:

Exactly one good electron (muon) is required in the e+jets (μ+jets) channel.

Jets:

At least four good jets are selected in the e+jets (μ+jets) channel. At least of them should be b-jet.

Photons:

Two good photons are required. If the photons have $\Delta R(l, \gamma) < 1.0$ with any good lepton, the events are dropped.

4.6.1 Signal Acceptance and Correction Factor

The signal acceptance is defined as the fraction of events falling into the fiducial region out of the total generated [17]:

$$A_i = \frac{N_{gen}^{fid,i}}{N_{gen}^{all}} \tag{4.1}$$

where N_{gen}^{all} is the total number of generated events and $N_{gen}^{fid,i}$ is the number of events inside the fiducial region i, with i running over the single lepton channel. The events inside fiducial region are selected by applying the selection for the fiducial region in the single lepton channel. **Table 3.10** shows the selected event yields in the fiducial region. An initial cut selects exact one electron or muon. The selected event yields are weighed by MC generator weight and pile up weight.

The correction factor is used to unfold the number of signal selected at reconstruction level $N_{reco,i}$ in channel i to the number of generated signal events in the fiducial region $N_{gen}^{fid,i}$ corresponding to channel i [17].

$$C_i = \frac{N_{reco,i}}{N_{gen}^{fid,i}} \tag{4.2}$$

The selected signal events at reconstruction level, using the $t\bar{t}\gamma\gamma$ event selection, are shown in the **Table 3.11**. The luminosity weight is not applied in this selection. The isolation γ_1 and γ_2 cuts in the **Table 3.11** mean the requirements of the selection which both photons have to be isolated.

Table 3.10 The event yields for particle-level signal sample in the e+jets and μ+jets channels, respectively. Only statistical uncertainties are included.

Process	e+jets	μ+jets
Initial	287.29 ± 0.56	289.18 ± 0.57
$N_\gamma = 2$	1.81 ± 0.04	1.76 ± 0.04
$N_{jets} \geqslant 4$	1.81 ± 0.04	1.76 ± 0.04
$N_{bjets} \geqslant 1$	1.78 ± 0.04	1.72 ± 0.04
$\Delta R(l, \gamma_1)$	1.53 ± 0.04	1.46 ± 0.03
$\Delta R(l, \gamma_2)$	1.11 ± 0.03	1.04 ± 0.03

Table 3.11 The signal yields for reconstruction-level in the e+jets and μ+jets channels, respectively. Only statistical uncertainties are included.

Process	e+jets	μ+jets
Initial	196.32 ± 0.21	181.65 ± 0.18
$N_\gamma = 2$	1.66 ± 0.04	1.51 ± 0.03
Isolation γ_1	1.04 ± 0.04	0.90 ± 0.03
Isolation γ_2	0.59 ± 0.02	0.49 ± 0.02
Truth matching γ_1	0.53 ± 0.02	0.45 ± 0.02
Truth matching γ_2	0.48 ± 0.02	0.42 ± 0.02
$N_{jets} \geqslant 4$	0.48 ± 0.02	0.42 ± 0.02
$N_{bjets} \geqslant 1$	0.43 ± 0.02	0.38 ± 0.02
$\lvert m(e, \gamma_1) - m(Z) \rvert > 5$	0.41 ± 0.02	-
$\lvert m(e, \gamma_2) - m(Z) \rvert > 5$	0.38 ± 0.02	-
$\Delta R(l, \gamma_1)$	0.30 ± 0.02	0.32 ± 0.02
$\Delta R(l, \gamma_2)$	0.23 ± 0.02	0.26 ± 0.02

Finally, **Table 3.12** summarizes the calculated signal acceptance and correction factors, using the particle level signal sample, in the single lepton channel.

Table 3.12 The event yields inside fiducial region, generated events and calculated signal acceptance and correction factors in the e+jets and μ+jets channels, respectively. Only statistical uncertainties are included.

Process	e+jets	μ+jets
$N_{gen}^{fid,i}$	1.11 ± 0.04	1.04 ± 0.03
N_{gen}^{all}	4171.16 ± 72.82	4171.16 ± 72.82
$N_{reco,i}$	0.22 ± 0.01	0.25 ± 0.01
Signal Acceptance	$0.00027 \pm (1.07 \times 10^{-5})$	$0.00025 \pm (8.4 \times 10^{-6})$
Correction Factor	0.21 ± 0.02	0.25 ± 0.02

4.7 Fiducial Cross Section Measurement

The number of generated events in the fiducial region is derived by subtracting background events from data and applying of the correction factor [17]. To calculate the fiducial cross section, this number is divided by the integrated luminosity. Using the expression 4.3, the fiducial cross section can be calculated. Index i runs over the single lepton channels:

$$\sigma_i^{fid} = \frac{N_{data,i} - N_{bkgs,i}}{L \times C_i} \tag{4.3}$$

Here:

$N_{data,i}$ - number of data events corresponding to the i channel

$N_{bkgs,i}$ - total number of background events corresponding to the i channel

L - total integrated luminosity

C_i - correction factor corresponding to the i channel

The predicted fiducial cross section can be calculated using the total cross section from theory prediction:

$$\sigma_i^{pred.fid} = \sigma_{theory}^{tot} \times A_i \tag{4.4}$$

Here:

A_i - signal acceptance corresponding to the i channel

σ_{theory}^{tot} - total cross section from theory prediction

The predicted fiducial cross sections for the $t\bar{t}\gamma\gamma$ process are calculated using the higher order cross section of $t\bar{t}\gamma$ process of 5.36 pb. The predicted values for the $t\bar{t}\gamma\gamma$ fiducial cross sections are a total of 1.44 ± 0.06 fb and 1.34 ± 0.05 fb with only statistical errors in the e+jets and μ+jets channels, respectively. The following table summarizes the predicted values and measured fiducial cross sections.

Table 3.13 The predicted and measured $t\bar{t}\gamma\gamma$ fiducial cross section in the e+jets and μ+jets channels, respectively. Also data events, predicted signal events and total backgrounds are shown.

	e+jets	μ+jets
N_{data}	28 ± 5.29	17 ± 4.12
N_{bkgs}	6.93 ± 2.70	3.75 ± 1.20
N_{sig}	11.15 ± 0.75	12.52 ± 0.84
Signal Acceptance	$(2.7 \times 10^{-4}) \pm (1.07 \times 10^{-5})$	$(2.5 \times 10^{-4}) \pm (8.4 \times 10^{-6})$
Correction Factor	0.21 ± 0.02	0.25 ± 0.02
Predicted $\sigma^{fid}_{t\bar{t}\gamma\gamma}$	1.44 ± 0.06 fb	1.34 ± 0.05 fb
Measured $\sigma^{fid}_{t\bar{t}\gamma\gamma}$	2.78 ± 0.82 fb	1.47 ± 0.49 fb

In the **Table 3.13** the total background N_{bkgs} is the sum of contributions of the prompt photon, fake photon, fake lepton and $t\bar{t}H$ background events. Predicted signal yields N_{sig} and data events N_{data} are selected using the single-lepton $t\bar{t}\gamma\gamma$ event selection in the single lepton channel as described in Section 4.3.

Statistical uncertainty for the fiducial cross section:

The expression 4.7 for statistical uncertainty of the fiducial cross section is derived from variance of the fiducial cross section as shown the following expression:

$$V(\sigma_i^{fid}) = (\frac{\partial \sigma_i^{fid}}{\partial N_{data}})^2 V(N_{data}) + (\frac{\partial \sigma_i^{fid}}{\partial N_{bkgs}})^2 V(N_{bkgs}) + (\frac{\partial \sigma_i^{fid}}{\partial C_i})^2 V(C_i) \qquad (4.5)$$

Using the standard deviation expression $\sigma(\sigma_i^{fid}) = \sqrt{V(\sigma_i^{fid})}$, the equation 4.5 can be re-written as follows:

$$\sigma(\sigma_i^{fid}) = \sqrt{(\frac{\partial\sigma_i^{fid}}{\partial N_{data}})^2\sigma^2(N_{data}) + (\frac{\partial\sigma_i^{fid}}{\partial N_{bkgs}})^2\sigma^2(N_{bkgs}) + (\frac{\partial\sigma_i^{fid}}{\partial C_i})^2\sigma^2(C_i)} \quad (4.6)$$

Then, by finding the derivatives the expression for the statistical uncertainty of the fiducial cross section can be written as:

$$\sigma(\sigma_i^{fid}) = \frac{1}{L \times C_i}\sqrt{\sigma^2(N_{data}) + \sigma^2(N_{bkgs}) + (N_{data} - N_{bkgs})^2(\frac{\sigma(C_i)}{C_i})^2} \quad (4.7)$$

where index i runs over the single lepton channels and $\sigma(N_{data})$, $\sigma(N_{bkgs})$ and $\sigma(C_i)$ are the statistical errors of each components as shown in the **Table 3.13**. Finally, using the equation 4.7 the $t\bar{t}\gamma\gamma$ fiducial cross sections with statistical uncertainties are measured:

$$\text{e+jets channel: } \sigma_{t\bar{t}\gamma\gamma}^{fid} = (2.78 \pm 0.82) \text{ fb}$$
$$\mu\text{+jets channel: } \sigma_{t\bar{t}\gamma\gamma}^{fid} = (1.47 \pm 0.49) \text{ fb}$$

Statistical uncertainty for the predicted fiducial cross section:

Using the following expression, the statistical uncertainty for the predicted fiducial cross section is estimated:

$$\sigma(\sigma_i^{pred.fid}) = \sigma_i^{pred.fid}\sqrt{(\frac{\sigma(\sigma_{theory}^{tot})}{\sigma_{theory}^{tot}})^2 + (\frac{\sigma(A_i)}{A_i})^2} \quad (4.8)$$

4.8 Systematic Uncertainties

Three sources of systematic uncertainties are considered in the $t\bar{t}\gamma\gamma$ cross section measurement. All sources are from the modelling uncertainties of the signal in the single lepton channel.

Parton shower and hadronisation uncertainty:

The uncertainty due to the parton shower and hadronisation is estimated by comparing the $t\bar{t}\gamma\gamma$ nominal samples produced using MadGraph + Pythia8, with Herwig7 showering the same MadGraph events [17]. As shown the expression 4.9 the relative difference on the signal acceptance and correction factors due to this systematic sources gives the showering systematic uncertainty on these factors.

$$Sys.Uncertainty = \frac{Sys.Value - Nominal}{Nominal} \tag{4.9}$$

where, the Nominal values and Sys.Values are the calculated acceptance and correction factor values with the $t\bar{t}\gamma\gamma$ nominal sample and with Herwig7 showering the same MadGraph events.

Table 3.14 The parton shower and hadronisation uncertainty.

Showering Uncertainty	Correction Factor	Signal Acceptance
	e+jets	
Nominal	0.148 ± 0.014	$0.00036 \pm (1.65 \times 10^{-5})$
Sys.Value	0.169 ± 0.015	$0.00025 \pm (1.25 \times 10^{-5})$
Sys.Uncertainty [%]	14.2 ± 13.9	30.6 ± 5.9
	μ+jets	
Nominal	0.170 ± 0.012	$0.00035 \pm (1.60 \times 10^{-5})$
Sys.Value	0.178 ± 0.016	$0.00025 \pm (1.25 \times 10^{-5})$
Sys.Uncertainty [%]	4.7 ± 11.8	2.86 ± 5.9

In the **Table 3.14** the statistical uncertainties of this systematics are calculated with the following expression which is derived from the substraction and division errors for the expression 4.9:

$$\sigma(Sys.Uncertainty) = \frac{(Sys.Value - Nominal)}{Nominal} \times \tag{4.10}$$

$$\sqrt{\frac{(\sigma^2(Sys.Value) + \sigma^2(Nominal))}{(Sys.Value - Nominal)^2}) + (\frac{\sigma(Nominal)}{Nominal})^2}$$

Initial and final state radiation uncertainty (ISR/FSR):

The uncertainty due to the ISR/FSR is estimated by comparing the $t\bar{t}\gamma\gamma$ nominal sample with the same $t\bar{t}\gamma\gamma$ MadGraph events produced using Pythia8 tunes with high or low QCD radiation activity [17]. As shown the expression 4.11, the relative difference of the the signal acceptance and correction factor values due to the up and down variations of the systematic sources gives the ISR/FSR systematic uncertainty on these factors.

$$Sys.Uncertainty(Up) = \frac{Up.Value - Nominal}{Nominal} \tag{4.11}$$

$$Sys.Uncertainty(Down) = \frac{Down.Value - Nominal}{Nominal}$$

The **Table 3.15** summarizes the calculated signal acceptance and correction factor values with the nominal sample and with the same $t\bar{t}\gamma\gamma$ MadGraph events produced using Pythia8 tunes with high or low QCD radiation activity in the single lepton channel. The corresponding statistical uncertainties are estimated with the previous expression 4.10.

Table 3.15 The signal acceptance and correction factor with the up and down variation of the initial and final state radiation sources.

ISR/FSR Uncertainty	Correction Factor	Signal Acceptance
	e+jets	
Nominal	0.21 ± 0.02	$0.00027 \pm (1.07 \times 10^{-5})$
Up.Value	0.23 ± 0.02	$0.00027 \pm (1.27 \times 10^{-5})$
Sys.Uncertainty(Up) [%]	9.5 ± 13.5	0
Nominal	0.21 ± 0.02	$0.00027 \pm (1.07 \times 10^{-5})$
Down.Value	0.20 ± 0.01	$0.00026 \pm (2.37 \times 10^{-5})$
Sys.Uncertainty(Down) [%]	4.8 ± 10.8	3.7 ± 9.6
	μ+jets	
Nominal	0.25 ± 0.02	$0.00025 \pm (8.4 \times 10^{-6})$
Up.Value	0.25 ± 0.02	$0.00026 \pm (1.25 \times 10^{-5})$
Sys.Uncertainty(Up) [%]	0	4.0 ± 6.0
Nominal	0.25 ± 0.02	$0.00025 \pm (8.4 \times 10^{-6})$
Down.Value	0.24 ± 0.03	$0.00024 \pm (2.21 \times 10^{-5})$
Sys.Uncertainty(Down) [%]	4.0 ± 14.0	4.0 ± 9.4

Renormalisation and factorization uncertainty:

To estimate this uncertainty renormalisation μ_r and factorisation μ_f scales varied by a factor of 2 or 1/2 with respect to the nominal sample value are used. The weights which includes these variation are applied in the nominal sample, instead of the variation samples.

The following table summarizes all systematic uncertainties on the correction factor and signal acceptance with the statistical uncertainties. To estimate a total systematic uncertainty of all systematic sources, the expression 4.12 is used.

$$\delta_{sys}^{tot}(C) = \sqrt{(\delta_{sys}^{Sho.}(C))^2 + (\delta_{sys}^{ISR/FSR}(C))^2 + (\delta_{sys}^{Scale}(C))^2} \tag{4.12}$$

$$\delta_{sys}^{tot}(A) = \sqrt{(\delta_{sys}^{Sho.}(A))^2 + (\delta_{sys}^{ISR/FSR}(A))^2 + (\delta_{sys}^{Scale}(A))^2}$$

Table 3.16 The systematic uncertainties on the signal acceptance and correction factor due to the up and down variation of the initial and final state radiation uncertainty sources.

Sources	Correction Factor	Signal Acceptance
	e+jets	
Showering uncertainty [%]	14.2 ± 13.9	30.6 ± 5.9
ISR/FSR uncertainty [%]	9.5 ± 13.5	3.7 ± 9.6
Scale variation uncertainty [%]	17.0 ± 8.5	26.9 ± 4.3
Total uncertainty [%]	25.9 ± 10.6	41.9 ± 5.19
	μ+jets	
Showering uncertainty [%]	4.7 ± 11.8	28.6 ± 5.9
ISR/FSR uncertainty [%]	4.0 ± 14.0	4.0 ± 9.4
Scale variation uncertainty [%]	7.1 ± 8.8	28.0 ± 4.3
Total uncertainty [%]	20.3 ± 5.0	41.1 ± 5.12

By finding the $\delta_{sys}^{Sho.}(C)$, $\delta_{sys}^{ISR/FSR}(C)$, $\delta_{sys}^{Scale}(C)$ derivatives from the expression 4.12 and then multiplying each statistical uncertainty the statistical uncertainty for the total systematic uncertainty can be written as follows:

$$\sigma(\delta_{sys}^{tot}(C)) = \frac{1}{\sqrt{[(\delta_{sys}^{Sho.}(C))^2 + (\delta_{sys}^{ISR/FSR}(C))^2 + (\delta_{sys}^{Scale}(C))^2]}} \times$$

$$\sqrt{[(\delta_{sys}^{Sho.}(C))^2 \times \sigma^2(\delta_{sys}^{Sho.}(C)) + (\delta_{sys}^{ISR/FSR}(C))^2 \times \sigma^2(\delta_{sys}^{ISR/FSR}(C)) + (\delta_{sys}^{Scale}(C))^2 \times \sigma^2(\delta_{sys}^{Scale}(C))]} \tag{4.13}$$

$$\sigma(\delta_{sys}^{tot}(A)) = \frac{1}{\sqrt{[(\delta_{sys}^{Sho.}(A))^2 + (\delta_{sys}^{ISR/FSR}(A))^2 + (\delta_{sys}^{Scale}(A))^2]}} \times$$

$$\sqrt{[(\delta_{sys}^{Sho.}(A))^2 \times \sigma^2(\delta_{sys}^{Sho.}(A)) + (\delta_{sys}^{ISR/FSR}(A))^2 \times \sigma^2(\delta_{sys}^{ISR/FSR}(A)) + (\delta_{sys}^{Scale}(A))^2 \times \sigma^2(\delta_{sys}^{Scale}(A))]} \tag{4.14}$$

Results:

The systematic uncertainties for the $t\bar{t}\gamma\gamma$ fiducial cross section measurement are calculated using the following expression:

$$\delta_{sys}^{tot}(\sigma^{fid}) = \sigma^{fid} \times \sqrt{(\delta_{sys}^{Sho.}(C))^2 + (\delta_{sys}^{ISR/FSR}(C))^2 + (\delta_{sys}^{Scale}(C))^2} \tag{4.15}$$

With this expression the $t\bar{t}\gamma\gamma$ fiducial cross sections including the systematic uncertainties can be written as:

$$\text{e+jets channel: } \sigma_{t\bar{t}\gamma\gamma}^{fid} = (2.78 \pm 0.82|_{stat} \pm 0.72|_{sys}) \text{ fb}$$
$$\mu\text{+jets channel: } \sigma_{t\bar{t}\gamma\gamma}^{fid} = (1.47 \pm 0.49|_{stat} \pm 0.29|_{sys}) \text{ fb}$$

To estimate the total systematic uncertainty of the predicted fiducial cross section, the signal acceptance uncertainty in the **Table 3.16** and k-factor uncertainty which is calculated in the $t\bar{t}\gamma$ analysis[17] as 20% in the single lepton channel are considered. Including these systematic uncertainties the predicted $t\bar{t}\gamma\gamma$ fiducial cross section can be written as:

$$\text{e+jets channel: } \sigma_{t\bar{t}\gamma\gamma}^{fid} = (1.44 \pm 0.06|_{stat} \pm 0.67|_{sys}) \text{ fb}$$
$$\mu\text{+jets channel: } \sigma_{t\bar{t}\gamma\gamma}^{fid} = (1.34 \pm 0.05|_{stat} \pm 0.61|_{sys}) \text{ fb}$$

Chapter 5

Summary and Outlook

In this thesis the fiducial and total cross section measurements of the $t\bar{t}\gamma\gamma$ production are performed with data collected by the ATLAS detector during 2015 and 2016 corresponding to an integrated luminosity of 36.1 fb^{-1} at a center-of-mass-energy of $\sqrt{s} = 13$ TeV, in the single lepton channels. In the single-lepton $t\bar{t}\gamma\gamma$ final state one lepton and at least four jets are requested, with at least one jet being b-tagged and two isolated photons with $p_T > 20$ GeV and $|\eta| < 2.37$.

A total of 28 ± 5.29 and 17 ± 4.12 data events are observed, and from simulation studies 11.15 ± 0.75 and 12.52 ± 0.84 signal events with statistical uncertainties are predicted in the electron and muon channels, respectively. Considering the fake photon, fake lepton and prompt photon backgrounds the background estimation is done. The largest contribution to the $t\bar{t}\gamma\gamma$ process comes from events with at least one fake photon which contribute to the fake photon background.

The total uncertainties for the $t\bar{t}\gamma\gamma$ fiducial cross sections are found to be 25.9 % and 20.3 % in the electron and muon channel, respectively. The $t\bar{t}\gamma\gamma$ fiducial cross sections within fiducial region are measured as:

$$\text{e+jets channel: } \sigma^{fid}_{t\bar{t}\gamma\gamma} = (2.79 \pm 0.82|_{stat} \pm 0.72|_{sys}) \text{ fb}$$
$$\mu\text{+jets channel: } \sigma^{fid}_{t\bar{t}\gamma\gamma} = (1.47 \pm 0.49|_{stat} \pm 0.29|_{sys}) \text{ fb}$$

The fiducial measurement in the muon channel is in good agreement with the predicted fiducial cross section within experimental uncertainties. But the measured fiducial cross section in the electron channel is larger than the predicted value.

Currently the measurement of the $t\bar{t}\gamma\gamma$ production total cross section is not posisble because of the limiting factor which is the k-factor in the $t\bar{t}\gamma\gamma$ signal sample. Further, by fixing the limiting factor it is possible to measure the total cross section. The measurement of the $t\bar{t}\gamma\gamma$ production cross section is an important in the background processes at the LHC.

Appendix

A Cut flow table

Event yields after applying the $t\bar{t}\gamma\gamma$ event selection.

Table 3.17 The event yields in the signal region

Selection	Signal MC	$W\gamma\gamma$	$Z\gamma\gamma$	Diboson+$\gamma\gamma$	Single Top+$\gamma\gamma$
e+jets					
Initial	13745.7 ± 21.01	311614 ± 703.67	284746 ± 609.87	18162.6 ± 117.81	28763.9 ± 101.84
$N_\gamma = 2$	246.17 ± 3.59	273.04 ± 19.16	2460.83 ± 55.90	26.91 ± 2.75	16.07 ± 3.11
Isolation γ_1	140.86 ± 2.70	156.52 ± 13.05	1413.3 ± 42.26	13.85 ± 2.17	4.38 ± 1.38
Isolation γ_2	73.77 ± 1.89	74.16 ± 8.32	976.35 ± 34.91	8.09 ± 1.29	1.77 ± 0.61
Truth matching γ_1	61.85 ± 1.75	68.06 ± 7.87	427.31 ± 19.84	2.44 ± 0.76	1.34 ± 0.53
Truth matching γ_2	51.55 ± 1.61	62.25 ± 7.51	99.29 ± 9.66	0.52 ± 0.38	0.24 ± 0.19
$N_{jets} \geq 4$	23.81 ± 1.11	1.05 ± 0.61	3.85 ± 1.33	0.01 ± 0.01	0.18 ± 0.18
$N_{bjets} \geq 1$	21.43 ± 1.06	0 ± 0	0.54 ± 0.60	0 ± 0	0.18 ± 0.18
$\lvert m(e,\gamma_1) - m(Z)\rvert > 5$ GeV	20.25 ± 1.04	0 ± 0	0.54 ± 0.60	0 ± 0	0.18 ± 0.18
$\lvert m(e,\gamma_2) - m(Z)\rvert > 5$ GeV	18.69 ± 1.00	0 ± 0	0.54 ± 0.60	0 ± 0	0.18 ± 0.18
$\Delta R(l,\gamma_1)$	14.89 ± 0.88	0 ± 0	0.54 ± 0.60	0 ± 0	0 ± 0
$\Delta R(l,\gamma_2)$	11.15 ± 0.75	0 ± 0	0.60 ± 0.60	0 ± 0	0 ± 0
μ+jets					
Initial	12875.4 ± 19.97	334282 ± 741.12	306280 ± 630.45	15204.2 ± 76.76	27507.3 ± 98.53
$N_\gamma = 2$	228.94 ± 3.41	259.21 ± 16.55	355.05 ± 19.87	12.56 ± 1.62	11.08 ± 1.75
Isolation γ_1	131.67 ± 2.59	136.77 ± 12.25	215.77 ± 15.78	5.89 ± 1.06	2.69 ± 0.74
Isolation γ_2	67.09 ± 1.84	67.22 ± 8.48	118.60 ± 11.53	3.28 ± 0.80	1.39 ± 0.53
Truth matching γ_1	56.19 ± 1.66	64.28 ± 8.23	115.90 ± 11.46	1.81 ± 0.64	1.00 ± 0.46
Truth matching γ_2	47.34 ± 1.54	63.99 ± 7.89	114.89 ± 11.40	1.63 ± 0.63	0.36 ± 0.25
$N_{jets} \geq 4$	20.68 ± 1.01	2.20 ± 1.02	3.29 ± 0.95	0.01 ± 0.01	0.18 ± 0.18
$N_{bjets} \geq 1$	18.69 ± 0.97	0.37 ± 0.37	1.14 ± 0.56	0 ± 0	0 ± 0
$\Delta R(l,\gamma_1)$	15.80 ± 0.92	0.37 ± 0.37	1.14 ± 0.56	0 ± 0	0 ± 0
$\Delta R(l,\gamma_2)$	12.52 ± 0.84	0.37 ± 0.37	0.57 ± 0.36	0 ± 0	0 ± 0

Table 3.18 The event yields in the signal region

Selection	$t\bar{t}H$	HFake	EFake	Fake lepton	Data
e+jets					
Initial	14.6 ± 1.94	3251890 ± 11779.4	3251890 ± 11779.4	1276840 ± 2283.88	4853250 ± 2203.01
$N_\gamma = 2$	7.36 ± 1.36	2559.02 ± 231.52	2559.02 ± 231.52	135.79 ± 47.69	5159 ± 71.82
Isolation γ_1	5.54 ± 1.21	1176.02 ± 147.78	1176.02 ± 147.78	-11.18 ± 31.64	2745 ± 52.39
Isolation γ_2	5.54 ± 1.14	724.40 ± 111.83	724.40 ± 111.83	-30.19 ± 22.04	1585 ± 39.81
Truth matching γ_1	5.54 ± 1.14	-21.61 ± 31.99	370.57 ± 63.11	-30.19 ± 22.04	1585 ± 39.81
Truth matching γ_2	5.54 ± 1.14	-25.11 ± 31.58	-0.02 ± 0.03	-30.19 ± 22.04	1585 ± 39.81
$N_{jets} \geq 4$	3.78 ± 0.98	0.47 ± 0.31	0.02 ± 0.02	-0.19 ± 3.23	61 ± 7.81
$N_{bjets} \geq 1$	5.1 ± 0.92	0.47 ± 0.31	0 ± 0	-0.30 ± 2.62	41 ± 6.40
$\lvert m(e,\gamma_1) - m(Z)\rvert > 5$ GeV	3.05 ± 0.90	0.47 ± 0.31	0 ± 0	0.12 ± 2.61	35 ± 5.91
$\lvert m(e,\gamma_2) - m(Z)\rvert > 5$ GeV	2.95 ± 0.9	0.47 ± 0.31	0 ± 0	0.68 ± 2.59	32 ± 5.65
$\Delta R(l,\gamma_1)$	2.23 ± 0.84	0.47 ± 0.31	0 ± 0	0.89 ± 2.58	30 ± 5.47
$\Delta R(l,\gamma_2)$	2.04 ± 0.81	0.47 ± 0.31	0 ± 0	1.10 ± 2.58	28 ± 5.29
μ+jets					
Initial	11.68 ± 1.79	2232100 ± 9835.32	2232100 ± 9835.32	151769 ± 1068.5	2990380 ± 1729.27
$N_\gamma = 2$	5.96 ± 1.32	528.22 ± 75.24	528.22 ± 75.24	12.36 ± 13.92	1712 ± 41.37
Isolation γ_1	4.7 ± 1.19	280.50 ± 65.56	280.50 ± 65.56	11.00 ± 10.83	896 ± 29.93
Isolation γ_2	3.89 ± 1.02	134.34 ± 43.95	134.34 ± 43.95	9.53 ± 10.63	459 ± 21.42
Truth matching γ_1	3.89 ± 1.02	22.76 ± 18.70	9.87 ± 1.69	9.53 ± 10.63	459 ± 21.42
Truth matching γ_2	3.89 ± 1.02	17.10 ± 18.62	0.67 ± 0.49	9.53 ± 10.63	459 ± 21.42
$N_{jets} \geq 4$	2.74 ± 0.88	0.42 ± 0.40	0 ± 0	-0.43 ± 0.88	32 ± 5.65
$N_{bjets} \geq 1$	2.55 ± 0.79	0.42 ± 0.40	0 ± 0	-0.60 ± 0.84	22 ± 4.69
$\Delta R(l,\gamma_1)$	2.41 ± 0.77	0.42 ± 0.40	0 ± 0	-0.56 ± 0.84	18 ± 4.24
$\Delta R(l,\gamma_2)$	2.14 ± 0.76	0.42 ± 0.40	0 ± 0	-0.54 ± 0.84	17 ± 4.12

B Kinematic Distributions

The electron, muon and jets transverse momentum and pseudo-rapidity distributions are plotted in the **Figure 2.28** after applying the $t\bar{t}\gamma\gamma$ selection in the signal region. In the event selection exactly one electron with $p_T > 25$ GeV and $|\eta_{clus}| < 2.47$ and one muon with $p_T > 25$ GeV and $|\eta_{clus}| < 2.5$ are considered. Also the jets having $p_T > 25$ GeV and $|\eta| < 2.5$ are selected.

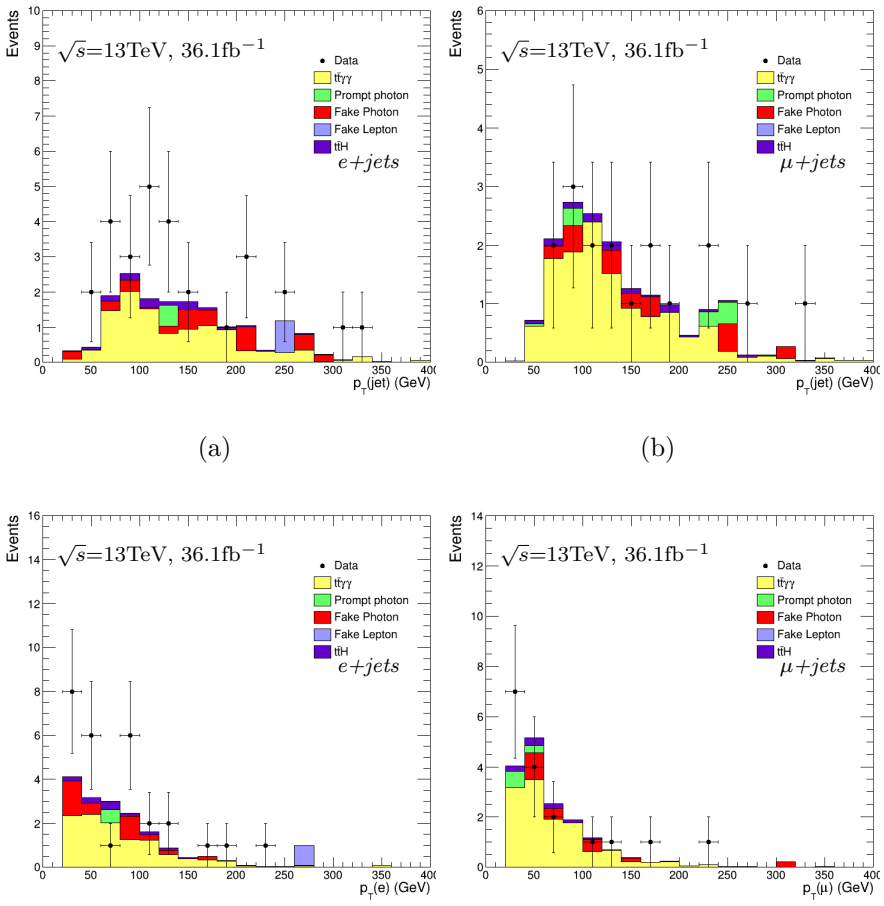

(a) (b)

(c) (d)

Figure 2.28 The distributions of the transverse momentum and pseudo-rapidity of the electron, muon and jets. The left upper plots in the a.) correspond to the electron and jets transverse momentum distributions and the left lower plots in the c.) shows to the electron and jets pseudo-rapidity distributions in the e+jets channel, the right plots correspond to the μ+jets channel, respectively.

Figure 2.29 shows the distributions of electron, jet and muon pseudo-rapidity in the single lepton channel.

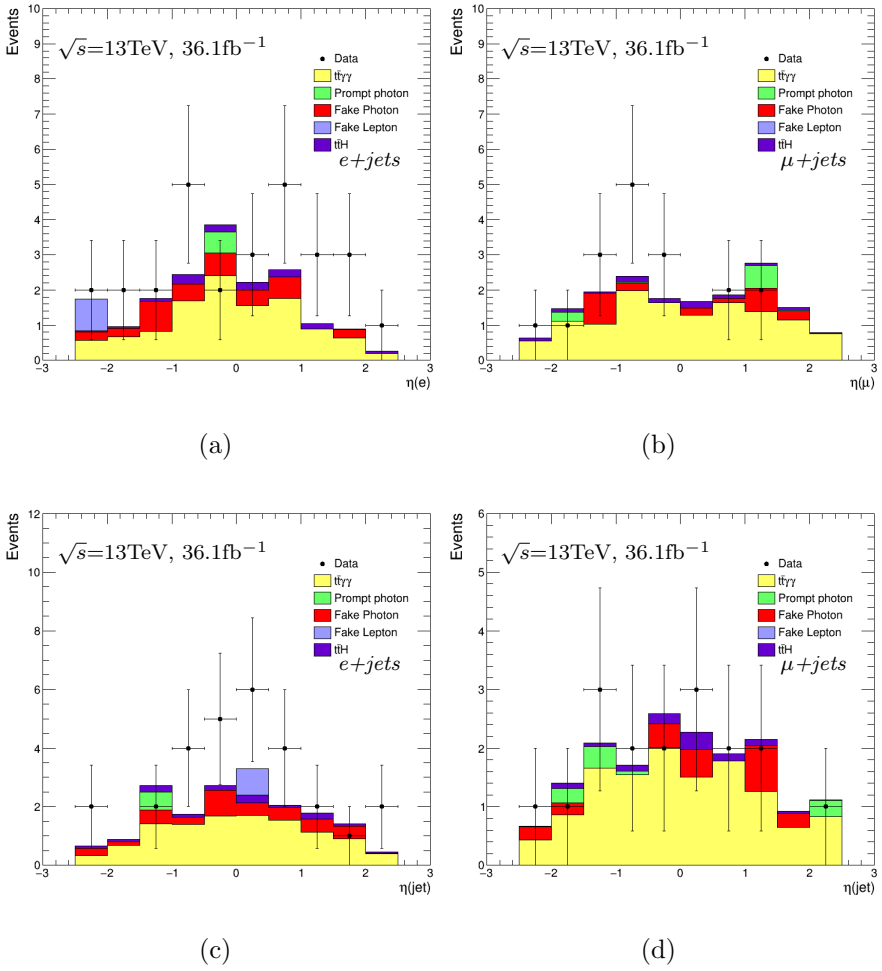

Figure 2.29 The distributions of the pseudo-rapidity of electron, muon and jet. The left two plots correspond to the e+jets channel, the right two plots to the μ+jets channel, respectively.

References

[1] Mark Thomson, (2013), Modern Particle Physics, Campbridge, UK: Cambridge University Press

[2] David Griffiths, (2008), Introduction to Elementary Particles, NeW York, NY: Wiley

[3] Ulrich Husemann, (2017), Progress in Particle and Nuclear Physics 95 48-97

[4] Nazar Bartosik, Categorisation of possible decay channels of a top-quark pair, including decays of W bosons to tau leptons [Online], Available: $http://bartosik.pp.ua/hep\_sketches/tt\_decay\_channels$

[5] The ATLAS Collaboration, (2011), Measurement of the inclusive $t\bar{t}\gamma$ cross section with the ATLAS detector, ATLAS-CONF-2011-153

[6] The accelerator complex, (2012), Available: $http://cds.cern.ch/record/1997193$

[7] Christiane Lefevre, (2008), The CERN accelerator complex [Online], Available: $https://cds.cern.ch/record/1260465?ln=de$

[8] Mike Lamont, (2013), Status of the LHC, Journal of Physics: Conference Series, Volume 455

[9] Elias Metral, (2016), Status: Prospects and Future Challenges LHC, PoS (LHCP216) 002

[10] Lucas Taylor, (2011), Detector overview [Online], Available: $http://cms.web.cern.ch/news/detector-overview$

[11] Ulrik Egede, (1998), Design of the ATLAS detector [Online], Available: $http://www.hep.lu.se/atlas/thesis/egede/thesis-node39.html$

[12] G Aad et al, (2008), ATLAS pixel detector electronics and sensors, JINST 3 P07007

[13] Dave Robinson, (2017), ATLAS Inner Detector [Online],
Available: $https://twiki.cern.ch/twiki/bin/viewauth/Atlas/InnerDetector$

[14] A. Abdesselam et al, (2006), The barrel modules of the ATLAS semiconductor tracker, Volume 568, Issue 2

[15] Roger Ruber, (2010), ATLAS magnet system [Online],
Available: $http://atlas-magnet.web.cern.ch/atlas-magnet/$

[16] McFayden, J. (2014), The ATLAS detector at the CERN large hadron collider, XVIII, 178 p. 97

[17] Caudron, J et al, (2017), Measurement of the $t\bar{t}\gamma$ production cross-section in pp collision at $\sqrt{13}$ TeV with the ATLAS detector, ATL-COM-PHYS-2017-673

[18] ROOT reference guide, (2018), ROOT TLorentzVector class [Online],
Available: $https://root.cern.ch/doc/master/classTLorentzVector.html$

Acknowledgements

I would like to thank the people who supported and helped me during my master studies.

Firstly, I would like to express my sincere gratitude to my supervisor Prof. Ivor Fleck for giving me the opportunity to work within the ATLAS experiment, with large datasets and for his guidance and all supports. I would like to thank to Dr. Yichen Li for his time to answer my questions and for his instructions helped me in all the time of this analysis. I am also thank Sara Ghasemi, for her time to read my thesis and for the suggestions and comments. Many thanks to Binish Batool for her helps and for her time to answer my questions. Many thanks to Amartya Rej and John Meshreki for their helps and their advices.

I would like to thank my familly for supporting me all the time.

Erklärung

Hiermit verschiere ich, dass ich die vorliegende Masterarbeit selbststndig verfasst und keiene anderen als die angegebenen Quellen und Hilfsmittel benuzt, sowie Zitate und Ergebnisse Anderer kenntlich gemacht habe.

Datum Unterschrift